Sensors and Actuators A 326 (2021) 112730

Contents lists available at ScienceDirect

Sensors and Actuators A: Physical

journal homepage: www.elsevier.com/locate/sna

Excitation-frequency determination based on electromechanical impedance spectroscopy for a laser-microfabricated cavitation microstreaming micromixer

Hyunjin Jeon, Kaba Abdi Mirgissa, Seonhyuk Baek, Kyehan Rhee, Dohyun Kim *

Department of Mechanical Engineering, Myongji University, 116 Myongji-ro, Yongin, 17058, Republic of Korea

ARTICLE INFO

Article history:
Received 4 December 2020
Received in revised form 14 March 2021
Accepted 30 March 2021
Available online 3 April 2021

Keywords:
Micromixer
Cavitation microstreaming
Flow visualization
Electromechanical impedance spectroscopy (EMIS)
Laser micromachining
Adhesive bonding

ABSTRACT

We *for the first time* propose and validate an electromechanical impedance spectroscopy (EMIS) technique to determine the resonance frequency (f_r) of micromixers for effective cavitation microstreaming. Theoretical f_r predictions of the oscillating bubble have been inaccurate because it was assumed that the bubble had a spherical shape even though bubbles are commonly trapped in low-profile air pockets, and thus their shapes are not spherical. Empirical excitation-frequency search has been employed but it was time-consuming and could overlook the exact value of f_r. Strong electromechanical coupling between a piezoelectric transducer and a microfluidic chip (i.e., a mechanical structure) allows straightforward, rapid f_r determination (~4.5 min) using EMIS. To validate the EMIS method, we compare microstreaming patterns generated by bubbles excited at four different resonance frequencies using a high-speed imaging setup: 1) $f_{r,B}$, the theoretical f_r assuming a spherical bubble, 2) $f_{r,Beq}$, the theoretical f_r based on the concept of an "equivalent spherical bubble" having a surface area equal to the vibrating air-water interface area, 3) $f_{r,Pf}$, the EMIS-based f_r of a piezoelectric transducer, and 4) $f_{r,Cf}$, the EMIS-based f_r of the microfluidic chip bonded with the transducer. After confirming that $f_{r,Cf}$ yields the strongest cavitation microstreaming, the air-pocket shape is designed with consideration of the bubble stability and mixing effectiveness. A micromixer chip with the designed air pockets is excited at $f_{r,Cf}$ and exhibits rapid homogenization (37.2 s) of diluted ink and deionized water in the mixing chamber of a substantial volume (61.9 μL). Additionally, an experimentally validated, adhesive-tape-supported laser microfabrication technique allows rapid prototyping (~10 min) of polymethyl methacrylate microfluidic chips with an excellent dimensional accuracy, machining resolution, and surface smoothness. We expect the proposed EMIS-based technique for resonance-frequency determination and the simple, rapid laser microfabrication method to be widely employed for bio-/chemical microfluidic applications in the near future.

1. Introduction

A mixer is an essential functional component of a microfluidic device. Mixing can play a vital role in the operation of microfluidic assays [1], examples of which include biochemical analyses (e.g., immunoassay [2], DNA hybridization [3]), enzymatic reaction (e.g., protein digestion [4]), and chemical synthesis (e.g., isotope preparation [5]). Convective mixing based on turbulent flows, which is common in macroscale, is not suitable because of the small Reynolds number (Re) inherent to microfluidic devices, characterized by microscopic dimensions [6–9]. Previous reviews highlighting a cornucopia of articles may indicate the importance of and interest in this topic [7–16].

Microfluidic mixers are typically classified into passive and active mixers [7–10,12,13,16]. A passive mixer relies on transversal diffusion between narrow laminae of liquid streams and/or chaotic advection caused by geometric effects [10,15,17]. The passive mixer does not require external energy other than pumping energy. Therefore it is simple to operate since the sole control parameter is flow rate. However, the fabrication of intricate obstacles (e.g., barrier [18] and pillar [19]), grooves (e.g., staggered herringbone groove [20] and slanted groove [21]), and three-dimensional (3D) structures (e.g., Tesla structure [22], crossing manifold [23], and twisted channel [24]) using conventional two-dimensional (2D) microfabrication techniques can be challenging [11]. Additionally, the obstacles and grooves may create dead volumes in the flow path [8,14]. For rapid mixing (i.e., effective mixing), high flow rates and

* Corresponding author.
E-mail address: dohyun.kim@mju.ac.kr (D. Kim).

https://doi.org/10.1016/j.sna.2021.112730
0924-4247/

consequently high pressures have been required in several cases [7,12,15,25]. Such high flow rates and pressures are unnecessary for most real-world microfluidic applications (Re<1) [10–12] and can cause rupture and leakage in microfluidic devices. Another critical problem linked to the passive mixer is the lack of control on the extent of mixing because only the flow rate can be adjusted [8,14]. If the fluid properties (e.g., viscosity) change, the mixing results can be significantly different [15].

An active mixer relies on disturbances from external force fields (e.g., magnetic, electrokinetic, acoustic, pressure, electrohydrodynamic, dielectrophoretic, thermal, and centrifugal) for mixing [7,10]. Therefore, an external power source and/or actuator is required, along with a pressure source that generates the flow. For some agitation methods, the integration of additional components (e.g., magnetic stir bars [26], magnetic particles [27], surface acoustic wave interdigitated transducers [28], liquid metal droplets [29]), heaters [30], or electrodes [31]) can be complex. Nevertheless, the active mixer may have a simpler geometry (e.g., a simple straight channel or a chamber geometry without patterns or obstacles) than its passive counterpart [7]. Additionally, an active micromixer (or a microfluidic device incorporating one) can operate in a more controlled manner than a passive mixer. The operating conditions of an active mixer (i.e., the extent of mixing) can be quickly adjusted by controlling the external force fields (e.g., frequency, intensity, and duration) without changing the design of the mixer [8,14], which would take significantly longer. Therefore, active mixing may be more suitable than passive mixing for biochemical assays such as nucleic-acid extraction [32], where precise control of mixing in multiple assay stages is required. Moreover, external agitation can drastically shorten the mixing time (i.e., effective mixing) [25], which can lead to a higher throughput and a more compact device. For the same reason, a microfluidic device incorporating an active micromixer can operate under low-flow-rate conditions (Re<1).

Acoustic-field-driven micromixers rely on the streaming generated by the acoustic resonance of an interface between a liquid and a solid (i.e., diaphragm) or between a liquid and a gas (i.e., bubble) [7–9,16,33]. Rayleigh streaming [34–36], cavitation microstreaming [37,38], Eckart streaming [39], and surface-acoustic-wave streaming [28,40,41] have been used for acoustic mixing applications [33]. The acoustic micromixer has several advantages over the other active micromixers. First, the microfabrication can be simpler than that for electrohydrodynamic, electrokinetic, dielectrophoretic (i.e., embedded electrodes), thermal (i.e., embedded heater), and magnetic micromixer (i.e., inserted magnetic stir bars or beads) because acoustic disturbances can be readily generated by an external piezoelectric actuator [33,37,41–43]. Second, acoustic mixing is less sensitive to the liquid properties than magneto-hydrodynamic mixing (i.e., electrolyte or ferrofluid) and electrokinetic mixing (i.e., electrolyte). Third, acoustic mixing is less sensitive to the surface properties than electrohydrodynamic and electrokinetic disturbances (i.e., electrode surface) as surface-property changes have minor effects on the acoustic-energy transmission. Fourth, the operation of an acoustic micromixer can be simple as it only requires an alternating-current (AC) signal source (and a power amp) connected to a piezoelectric actuator [8]. In contrast, pressure-field-based mixing requires the control of multiple pressure sources and valves. Magneto-hydrodynamic-based mixing requires the simultaneous application of electric and magnetic fields [7,12]. Lastly, acoustic mixing is effective [8], as evidenced by exceptionally rapid mixing (as fast as a few milliseconds) [7].

Cavitation microstreaming harnesses strong circulatory flows induced by the viscous dissipation of acoustic energy around stably vibrating microbubbles [33,38]. When a bubble is excited near its resonance frequency, the streaming velocity is amplified [44] and can be orders of magnitude higher than that of a vibrating solid particle of a similar size; the streaming velocity of an oscillating bubble with a radius of 250 μm reaches 100–400 μm/s [45]. As mentioned earlier, the advantages of cavitation microstreaming include exceptionally fast mixing [42], easy implementation using a piezoelectric transducer glued to a micromixer [37], and the scalability of the mixing volume (from a few nanoliters to milliliters [33]). Thus, micromixers based on cavitation microstreaming have been actively studied in the microfluidics community [35,37,42,46–50]. Various applications, including DNA hybridization [51,52], pH sensing [53], and colorimetric protein assays [54], have been demonstrated.

For effective mixing, a bubble should be excited at its resonance frequency (f_r). In most of the previous studies, the Rayleigh-Plesset equation [42,44,50,55] or the simpler Minnaert's equation was used to determine the resonance frequency [37,45,52,55]. Both equations assume a freestanding and perfectly spherical bubble. However, in previous studies, the bubbles were typically not freestanding and formed inside grooves cut out of microchannel/chamber wall or a ceiling (i.e., air pockets) for stability. Therefore, trapped bubbles usually consist of a convex air-liquid interface and rectangular air-solid interfaces of a low profile (as the height of a microfluidic device is typically far smaller than the other dimensions). Moreover, the length of the air-water interface tends to change from excitation to excitation [48,54]. Consequently, accurate calculation of a bubble resonance frequency is not straightforward [52,53]. Previously, some bubbles were excited at theoretical f_rs, assuming aspherical shapes. However, whether exciting at the theoretical f_rs yields the most effective mixing was not experimentally confirmed [37,51]. Conversely, without relying on theory, an empirical search within a frequency range was performed by monitoring generated streaming patterns [42,47,53,56]. However, this type of empirical approach can be time-consuming and can fail to find a true resonance frequency.

In this work, we propose a systematic approach for determining excitation frequency. First, as described earlier, we noted that only the air-liquid interface region (i.e., cylindrical paraboloid) of a trapped bubble could vibrate under excitation. Therefore, we estimate the "effective radius" of an imaginary spherical bubble having the same area as the vibratable air-liquid interface. This radius is substituted into the Rayleigh-Plesset equation to calculate the equivalent bubble-resonance frequency. Second, we consider the fact that a micromixer chip is a mechanical structure that can vibrate in bending motion when excited by a bonded piezoelectric transducer. It is hypothesized that resonant flexural vibration can result in the maximum deformation of air pockets, maximizing the oscillation amplitude of the bubbles trapped therein. Electromechanical impedance spectroscopy (EMIS) of the bonded piezoelectric transducer allows the monitoring of the mechanical behavior through electromechanical coupling [57]. The resonance frequencies of various mechanical structures have been measured using the EMIS method [58–63].

Here we propose to use EMIS, *for the first time*, to determine the resonance frequency of a micromixer chip. The micromixer chip was excited at the following four different frequencies: 1) the theoretical resonance frequency of a freestanding spherical bubble, 2) the theoretical resonance frequency of an equivalent spherical bubble whose area is equal to the area of an oscillating air-water interface, 3) the EMIS resonance frequency of the piezoelectric transducer, and 4) the EMIS resonance frequency of the micromixer chip. The streaming patterns of an oscillating bubble excited at the four frequencies were generated using a custom high-speed imaging setup. The streaming patterns were examined to determine which excitation frequency yielded the strongest cavitation microstreaming, thereby resulting in the most effective mixing.

We opted for a tape-assisted laser-machining technique for microfabrication of our micromixer chip. Laser micromachining

is suitable for the rapid prototyping of a polymer microfluidic device because direct writing using focused laser ablation has several advantages, including 1) no need for a cleanroom, 2) a rapid turnaround time without the need for a photomask or master-mold manufacturing, 3) contactless machining without tool wears or impact damages to a substrate, 4) the capability of machining non-planar structures, 5) the semi-3D fabrication capability, and 6) straightforward combination with other microfabrication techniques [64,65]. CO_2 lasers (wavelength of 10.6 μm) have been widely used for direct machining of polymethyl methacrylate (PMMA), a popular transparent, biocompatible polymeric substrate for microfluidic devices [66–71]. Of the various bonding techniques for polymer substrates, pressure-sensitive double-sided tapes have often been used because of the low cost, the wide selection of thickness and liner materials, the capability of bonding two heterogeneous surfaces [72], and the high bond strength [73]. Tape-based bonding allowed the rapid, straightforward fabrication of complex, multilayer structures [68,74–76]. In some cases, double-sided tapes have been used as functional interlayers incorporating microfluidic features such as via holes, microchannels, and cavities [66,68,70–73]. Sometimes, the tapes were pre-pasted to a polymer sheet to form a composite sheet. Subsequently, the composite sheet was cut to avoid cumbersome manual alignment of the tapes and polymer sheet [67,69,74].

In this work, pressure-sensitive double-adhesive tapes were pre-pasted to a thin PMMA sheet (250 μm), and the composite sheet was cut through to form an intermediate layer having microfluidic features such as a chamber and channels. The intermediate layer was later sandwiched between a top layer with fluidic interfaces and a bottom layer with a piezoelectric transducer to complete the microfluidic chip. The main contribution of this study is the optimization of the laser-machining parameters for the composite layer, i.e., the power, speed (i.e., feed rate), and frequency [77,78]. The optimization goals were a high machining resolution (<200 μm) for microfluidic-feature patterning, a smooth cut surface for minimal sporadic bubble trapping, and a small contour error for precise machining of designed features in the composite sheet [79]. To achieve these goals, we performed a systematic optimization of the machining parameters.

2. Theory

2.1. Bubble resonance frequency

Assuming small-amplitude vibration, no dissipative loss (e.g., viscous damping or heat conduction), and no surface tension, the Minnaert resonance frequency f_M of a spherical bubble freestanding in liquid (i.e., unattached to a solid surface as depicted in Fig. 1a) is expressed as follows [55]:

$$f_M = \frac{1}{2\pi R_o}\sqrt{\frac{3\kappa p_o}{\rho}}, \tag{1}$$

where R_o is the radius of the bubble, κ is the polytropic constant of gas inside the bubble (= 1.4 for air), p_o is the hydrostatic pressure of the liquid (typically atmospheric pressure of 101.325 kPa), and ρ is the density of the liquid (998.2 kg/m^3 at 20 °C for water). Similarly, the Rayleigh-Plesset equation gives the resonant frequency $f_{r,B}$:

$$f_{r,B} = \frac{1}{2\pi R_o\sqrt{\rho}}\sqrt{3\kappa\left(p_o + \frac{2\sigma}{R_o} - p_v\right) - \frac{2\sigma}{R_o} + p_v - \frac{4\eta^2}{\rho R_o^2}}, \tag{2}$$

where p_v is the vapor pressure, σ is the surface tension, and η is the viscosity of the liquid. If the viscous damping is negligible (i.e., $4\eta^2 \ll \rho {R_o}^2$, which is typical for the millimeter-scale bubbles considered here) and the vapor pressure is disregarded (for water, p_v = 2.3 kPa at 20 °C is negligible compared with p_o = 101.325 kPa), the following equation is applicable [44,55]:

$$f_{r,B} = \frac{1}{2\pi R_o\sqrt{\rho}}\sqrt{3\kappa\left(p_o + \frac{2\sigma}{R_o}\right) - \frac{2\sigma}{R_o}} \tag{3}$$

If Eq. (3) is further simplified by disregarding the surface tension (σ = 0.07286 N/m at 20 °C), it reduces to the Minnaert equation Eq. (1). The resonance frequency of a bubble has been calculated using either Minnaert's equation [37,45,52] or the Rayleigh-Plesset equation [42,50].

For improved stability and predetermined position, a bubble is commonly trapped in an air pocket (Fig. 1b), which is a rectangular or circular groove cut out of a microchannel/microchamber wall (i.e., horizontal arrangement) or a ceiling (i.e., vertical arrangement). Therefore, a trapped bubble consists of a small portion of a convex air-water interface that can generate flow and the remaining air-solid interface that cannot generate flow. Moreover, these air pockets generally have low aspect ratios (AR). Nevertheless, a freestanding spherical bubble was assumed for resonance-frequency calculation in some previous studies. The resonance frequency was calculated using either the radius of the circular air pocket (horizontal arrangement) or the radius of the circular air-pocket opening (vertical arrangement), but the spherical bubble assumption was not experimentally validated [37,51,52]. Some authors noted that this assumption was inaccurate [52]. In other cases, which were seemingly more accurate, the curvature of an air-water interface (Fig. 1b) was extrapolated to determine the bubble radius R_o for Eq. (3) [42,50]. However, this approach still does not reflect the fact that the solid air-pocket body cannot generate flow. Thus, the authors had to experimentally search for the true resonance frequency by observing streaming patterns while modifying excitation frequency near the theoretical value [42,50]. Therefore, using Eq. (1) or (3) with an extrapolated radius or the radius of an air pocket may not be a reliable method of calculating the resonance frequency. An attempt was made to derive an analytical expression for the resonance frequency of a trapped bubble [80], considering the non-flow-generating part of an air pocket. However, the equation did not include the hydrostatic pressure term p_o, which is critical in determining the work done by an oscillating bubble [44,55], and assumed a near flat air-water interface in contrast to its apparent convexness. Thus, the equation may not accurately predict the resonance frequency. Hence, some authors completely averted theoretical predictions and performed empirical searches within a frequency range [47,53,56].

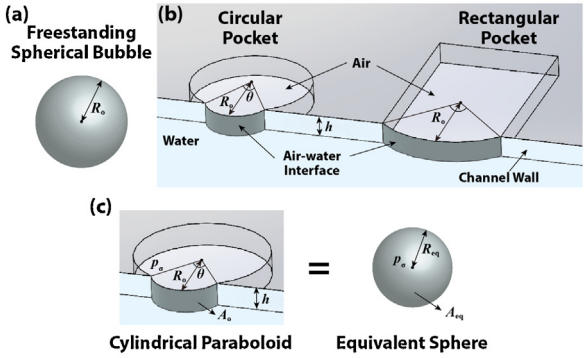

Fig. 1. Schematics of (a) a freestanding spherical bubble and (b) air-water interfaces formed on circular and rectangular air pockets. The interfaces are characterized by the radius of curvature R_o, angle θ, and height h. (c) The concept of the equivalent spherical bubble, whose surface area is equal to the surface area of the cylindrical paraboloid air-water interface, was used to calculate the resonance frequency using the Rayleigh-Plesset equation.

As a rigorous mathematical derivation of a resonance-frequency equation is not among the objectives of this study, we propose a first-degree estimation based on the concept of the "equivalent bubble radius." The Rayleigh-Plesset equation is derived from the equality between the kinetic energy of a liquid medium around a vibrating bubble and the work done by the surrounding pressure, which is related to the hydrostatic pressure p_o, small-amplitude-oscillating pressure $P(t)$, surface tension σ, and bubble radius R_o, as indicated by Eq. (4.60) of Ref. [55]. We assume that the pressure of a bubble trapped in an air pocket is uniform, that the air-water interface has the shape of a cylindrical paraboloid with a radius of curvature R_o, and that the amplitude of vibration is much smaller than R_o (i.e., small-amplitude vibration). We also assumed that the kinetic energy of the water surrounding a vibrating paraboloid and the work done by it are similar to those of a spherical bubble having the same surface area. Thus, we may be able to determine R_{eq}, the radius of a spherical bubble whose area A_{eq} is equal to the paraboloid area A_o, and substitute it into Eq. (3) to calculate the equivalent resonance frequency $f_{r,Beq}$. For the cylindrical paraboloid of radius R_o, angle θ, and height h, as illustrated in Fig. 1c, R_{eq} can be calculated as follows:

$$A_{eq} = 4\pi R_{eq}^2 = A_o = R_o \pi \theta h,$$
$$R_{eq} = \frac{1}{2}\sqrt{R_o \theta h} \tag{4}$$

After R_{eq} is substituted into Eq. (3), $f_{r,Beq}$ can be determined. The capillary-pressure term $2\sigma/R_o$ should be replaced with σ/R_o (not σ/R_{eq}), considering the original cylindrical paraboloid shape. The capillary pressure of a cylindrical paraboloid p_σ can be expressed as follows:

$$p_\sigma = \sigma\left(\frac{1}{R_1} + \frac{1}{R_2}\right) = \sigma\left(\frac{1}{R_o} + \frac{1}{\infty}\right) \simeq \frac{\sigma}{R_o}, \tag{5}$$

where R_1 and R_2 represent the two principal radii of curvature. Finally, $f_{r,Beq}$ can be expressed as follows:

$$f_{r,Beq} = \frac{1}{2\pi R_{eq}\sqrt{\rho}}\sqrt{3\kappa\left(p_o + \frac{\sigma}{R_o}\right) - \frac{\sigma}{R_o}} \tag{6}$$

Because this expression is a first-degree approximation, it was experimentally confirmed by comparing the streaming pattern generated at $f_{r,Beq}$ with those generated at $f_{r,B}$ (the resonance frequency calculated using R_o) and two other resonance frequencies experimentally obtained via the EMIS technique (refer to Sections 3.4-3.6 for more details).

2.2. Electromechanical impedance spectroscopy for resonance-frequency determination

The piezoelectricity of a piezoelectric material, such as lead-zirconate-titanate (PZT) ceramic, is characterized by the generation of voltage when the material is subjected to mechanical strain and conversely the generation of mechanical strain in response to an external voltage. Because of the strong electromechanical coupling, the mechanical behavior of a piezoelectric material affects the electrical behavior, particularly in the form of electrical impedance. Therefore, the mechanical behavior of a piezoelectric material can be studied by measuring the electrical impedance using an impedance analyzer [57]. In some sense, a piezoelectric material functions as an actuator and a sensor simultaneously (i.e., piezoelectric transducer).

The same principle can also apply when a piezoelectric transducer, such as a thin-film PZT disc, is bonded to a mechanical structure such as a microfluidic chip (Fig. 2a). Electromechanical coupling allows the mechanical behavior of the bonded structure to be analyzed [61] by correlating the mechanical impedance (or compliance) of a structure with the electrical impedance sensed by the piezoelectric transducer (Fig. 2b). When the AC current I is applied to a piezoelectric transducer attached to one side of a structure (i.e., unimorph arrangement), flexural vibration occurs. This vibration generates a measurable voltage V across the transducer output with a phase angle θ that is a function of frequency. By examining the complex impedance $\boldsymbol{Z}=\boldsymbol{V}/\boldsymbol{I}$ for peaks of the magnitude $|\boldsymbol{Z}|$ and phase θ over a frequency band of interest, the mechanical resonance frequency f_r of the structure can be determined [62]. This type of impedance-based study of mechanical behavior has been widely used in the field of structural health monitoring (SHM) [61,63].

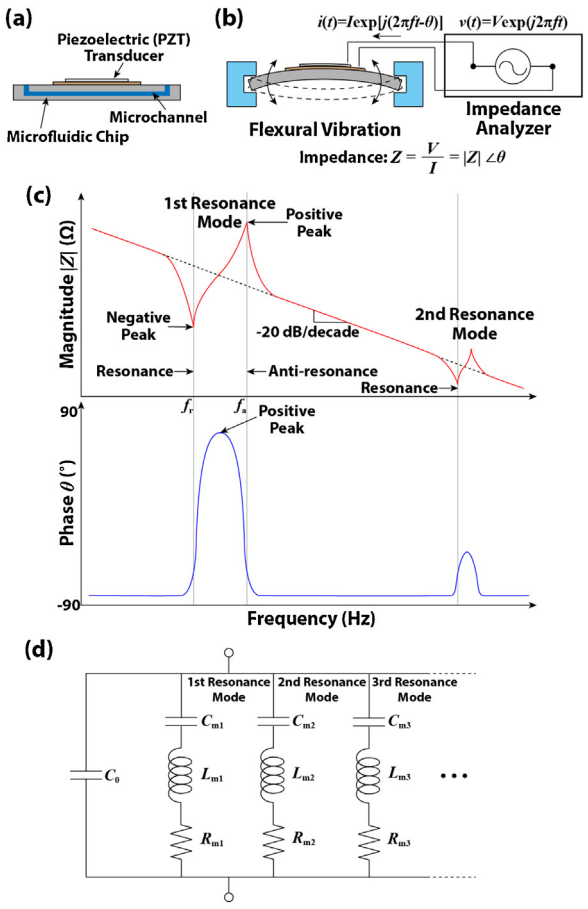

Fig. 2. Concept of resonance-frequency determination through electromechanical impedance spectroscopy (EMIS). (a) Piezoelectric diaphragm, which acts as an actuator and a sensor simultaneously, is bonded to a microfluidic chip. (2) AC voltage $v(t)$ and current $i(t)$ across the piezoelectric transducer are measured using an impedance analyzer to obtain an impedance spectrum. (3) Typical impedance plot for a piezoelectric transducer exhibits the mode-specific "resonance" and "anti-resonance" peaks in the magnitude plot and a positive peak (from -90°) in the phase plot. The piezoelectric transducer is usually excited at the "resonance" frequency f_r for the maximum-amplitude vibration. (4) Butterworth-Van Dyke (BVD) model includes an electrical circuit component C_o, and equivalent mechanical circuit components C_m, L_m, and R_m constituting an impedance signature for each vibration mode.

The resonance behavior expressed by the electrical impedance manifests as a local minimum "resonance," followed by a local maximum "anti-resonance" in the magnitude $|\boldsymbol{Z}|$, and a local maximum at a phase angle θ between the resonance frequency f_r and anti-resonance frequency f_a (Fig. 2c). At resonance, a large strain occurs, leading to a substantial change in the capacitance of the piezoelectric material. This resonance behavior results in the effective flow of charges (i.e., high current) in and out of the material during a vibration cycle, reducing impedance (i.e., local minimum). At anti-resonance, mechanical resonance also occurs. However, the overall strain is lower owing to the symmetry of the electric-field-induced

stains (i.e., tensile and compressive strains compensate each other). Thus, on average, there is little or no change in capacitance, and the flow of the charge is ineffective (i.e., low current). Therefore, an increase in impedance is observed (i.e., local maximum) at anti-resonance [57,81]. For the maximum vibration, a piezoelectric transducer is typically driven at its resonance frequency f_r [82]. Each mechanical resonance mode (e.g., flexural, radial, thickness modes) and its harmonics (e.g., 2nd, 3rd, 4th, and higher) are manifested as a pair of resonance and anti-resonance in electrical impedance. Because each resonance can be expressed in a distinct impedance signature as a function of the frequency, a Butterworth-Van Dyke (BVD) model of an equivalent circuit, consisting of an electrical capacitance C_o, and a mechanical resistance R_m, capacitance C_m and inductance L_m (Fig. 2d), can be constructed [83]. The material properties of a piezoelectric transducer can also be extracted by fitting an experimentally obtained impedance curve to a BVD model [83,84].

For the first time, we used the EMIS technique to determine the fundamental flexural resonance mode of a micromixer chip bonded with a piezoelectric transducer and to drive the structure at this mechanical resonance frequency for maximizing the flexural vibration amplitude. This resulted in strong bubble oscillation, which allowed effective cavitation microstreaming.

3. Experimental

3.1. Device design

We designed two types of microfluidic chips: the "EMIS chip" for the study of EMIS-based excitation-frequency determination and the optimization of the air-pocket shapes, and the "micromixer chip" for actual mixing experiments. As shown in Fig. 3a, each chip consisted of three functional layers, all made of PMMA: a top layer with fluidic interfaces, a chamber layer with microfluidic features, and a blank base layer for attaching a PZT transducer.

The most critical part of these microfluidic chips is the chamber layer housing a mixing chamber and air pockets situated on its perimeter. For the EMIS chip, two air pockets were positioned at the top and bottom so that unobstructed streaming visualization was achieved for validation of our EMIS technique (Fig. 3b). Using this EMIS chip, the design of the air pockets was experimentally determined for the stability of trapped bubbles and effectiveness of mixing (further detail is given in Section 3.7.). For the micromixer chip, six air pockets were evenly placed along the chamber perimeter to guarantee effective mixing (Fig. 3c). The detailed design of each layer is described in Appendix A.

3.2. Microfabrication

We used CO_2 laser machining and pressure-sensitive-tape-based adhesive bonding for the rapid prototyping of the EMIS chip and micromixer chip. Our key contribution is to develop a method of machining a PMMA sheet pre-pasted with pressure-sensitive tapes on both sides using experimentally optimized laser cutting for the chamber layer (Fig. 3b,c). The PMMA sheet and tapes were self-aligned after cutting and ready for bonding to the top and base layers without a tedious PMMA-tape alignment. The PMMA-tape composite layer was machined for microfluidic features using experimentally optimized laser cutting parameters (See Section 3.3 for detail). A PZT transducer, so-called disc bender, was super-glued to the base layer, which was made of white PMMA for high-contrast visualization of cavitation microstreaming.

A notable advantage of our tape-supported laser microfabrication method is that the adhesive, which can adsorb biomolecules, does not protrude between sandwiched PMMA layers. Moreover,

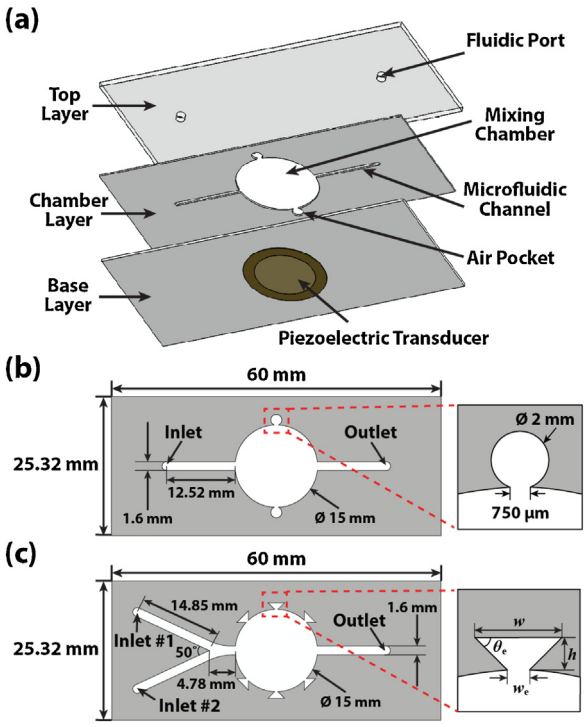

Fig. 3. Design of the microfluidic chips (more details are given in Appendix A). (a) Exploded view of a micromixer chip consisting of three layers: the top layer with fluidic interfaces, the chamber layer with microfluidic features, and the blank base layer bonded with a piezoelectric transducer. (b) Schematic of the chamber layer for the EMIS-based excitation-frequency determination and optimization of the air-pocket shape. Circular air pockets with a diameter of 2 mm and entrance width of 750 µm are situated at angles of 90° and 270° of the chamber (only circular air pockets are shown for brevity, but rectangular, triangular, and inverted-triangular air pockets were also designed). The chamber was connected to the inlet/outlet ports via 12.5 mm × 1.6 mm microchannels. (c) Schematic of the chamber layer for the mixing experiments. Two channels (14.85 mm × 1.6 mm) from inlets #1 and #2 brought two liquids into the mixing chamber, which was also connected to an outlet channel (12.5 mm × 1.6 mm). The six inverted-triangular air pockets with height h, base width w, entrance width w_e, and entrance angle θ_e, were situated at 45°, 90°, 135° 225°, 270°, and 315° for effective mixing within the microchamber.

by enclosing the microfluidic features of the chamber layer with smooth PMMA surfaces (i.e., top and base layers), the area of a rough surface can be minimized [85]. In contrast, laser engraving leaves a raked, significantly rough bottom surface that is prone to biomolecule adsorption [86,87]. Lastly, Luer-Lok compatible fluidic interfaces were glued to the top layer. After completion of microfabrication, the height of the microchamber was measured to be 350 µm, as defined by the composite-layer thickness. The volume of the chamber was 61.9 µL excluding those of air pockets. The entire fabrication process from CAD design to a complete chip took only ~10 min. It is faster than the polydimethylsiloxane (PDMS) or replication-based polymer microfabrication processes (e.g., hot embossing and injection molding) [64,65,88]. The detailed microfabrication process is described in Appendix A.

3.3. Optimization of laser-cutting parameters

The adjustable cutting parameters of the CO_2 laser machine, i.e., power (P, %), speed (S, %), and frequency (F, Hz), were systematically and experimentally optimized for the tape-PMMA-tape composite sheet. The goal of the optimization was to obtain: 1) a small kerf width (KW, <200 µm) for microfeature machining (>400-µm feature size), 2) smooth surfaces of cut sidewalls to minimize sporadic bubble trapping and biomolecular adsorption, and 3) a small con-

tour error for the accurate machining of designed microfeatures in the tape-PMMA-tape composite sheet.

For the KW optimization, cuts of 3-mm straight lines were made with varying P, S, and F values (Fig. 4a). The resulting KW values were measured using image analysis. The images were captured using an upright microscope BX50 (Olympus, Tokyo, Japan) equipped with a CoolSNAP HQ^2 camera (Teledyne Photometrics, Tucson, AZ, USA) and Metamorph software (Molecular Devices, San Jose, CA, USA). Subsequently, the KW was measured using the ImageJ software (NIH, Bethesda, Maryland, USA) and a microscope-stage calibration slide (TS-M1, AmScope, Irvine, CA, USA). The cutting conditions that yielded KW values less than 200 μm were selected.

For contour-error optimization, we selected the cutting conditions that maximized the roundness of a target circle (2 mm in diameter). Because of an imbalance between the x- and y-axis dynamics of servo systems that carry laser optics, there is always an error between a designed trajectory (i.e., laser-beam trajectory) and the actual trajectory (Fig. 4b) [79]. In general, the contour error tends to increase with an increase in the speed (or "feed rate") of the servo systems. A simple method of characterizing the contour error is to measure the roundness of a cut circle. One of the roundness metrics that we opted for was the aspect ratio (AR), i.e., the ratio of the major axis to the minor axis lengths. AR closer to 1 indicates that the actual cut is close to a perfect circle. Owing to the inherent roughness of CO_2 laser-machined PMMA surfaces, other metrics such as least-square circle (LSC) were not used in this work [89]. If AR was less than 1.06, the contouring performance was considered acceptable, and the corresponding cutting parameters were taken. For AR measurement, a grayscale image of a cut circle was captured using the BX50 microscope. The image was imported to Photoshop (Adobe, San Jose, CA, USA) to fill the inside of the circle boundary with black color so that the inside area (black) could be distinguished from the outside area (white). The processed image was subsequently imported to ImageJ, and the Threshold tool was used to extract the outline of the boundary. Finally, the Analyze Particles tool in ImageJ was used to calculate AR.

Lastly, for surface-roughness optimization, rectangular pieces (10 mm × 12 mm) were cut with different cutting parameters (Fig. 4c). One of the four cut edges was examined using an inverted microscope IX-70 (Olympus) equipped with a Zyla 5.5 camera (Andor Technology, Belfast, UK) after the workpiece was placed vertically with a slide insert (I-3091, ASI, Eugene, OR, USA). The surface roughness was qualitatively evaluated according to the area occupied by microscopic surface-roughness features. Blister-like features were observed throughout the surface, depending on the cutting conditions. The blister-like features generated strong background fluorescence, similar to the tapes used in this work, whereas the non-blistered regions did not exhibit a notable fluorescence signal (insets in Fig. 4c). A U-MWU2 filter set (Olympus) was used for the background-fluorescence observation. The background fluorescence from the tapes and blisters helped us theorize that the heat from the laser ablation vaporized the tape, which was later solidified on the PMMA surface, appearing as irregular blister-like features. If the area covered by the blisters accounted for less than 20 % of the entire surface, we considered the corresponding cutting condition to be acceptable.

The overall optimization process began with the KW measurement. A 3-mm straight cut was created for a parameter space of F=(1000, 2000, 3000, 4000, 5000) Hz; P=(3, 4, 5)%; and S=(1, 3, 5, 7, 9)%. The resulting KWs were measured. The laser machine could not cut through the sample using some low-power and high-speed combinations, and these combinations were discarded. Next, the combinations that did not satisfy the condition of a blister-covering area of <20 % or the roundness condition of

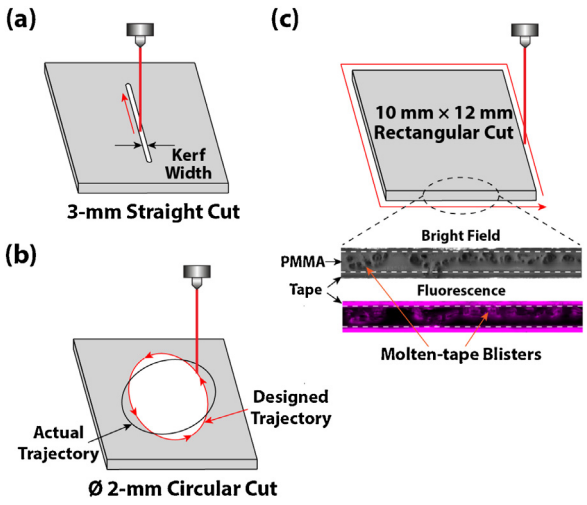

Fig. 4. Cutting parameter optimization. (a) Schematic of a 3-mm straight cut in the tape-PMMA-tape composite sheet for kerf-width optimization. (b) Schematic of the 2-mm-diameter target circle for contour-error optimization. The actual cut trajectory tended to be elliptical as the speed increased. (c) Schematic of a 10 mm × 12 mm rectangular piece for surface-roughness optimization. The surface roughness was qualitatively assessed according to the area covered by molten-tape blisters on one of the four cut sidewalls of the piece. The inset bright-field image and fluorescence image imply that the blisters had strong background fluorescence, similar to that of the tape, suggesting the origin of the blisters.

AR < 1.06 were discarded. Among the remaining parameter combinations, the one that yielded the smallest KW was selected as optimal. The 1-mm-thick top layer and 0.5-mm-thick base layer did not have critical microfeatures, except for a 2-mm-diameter inlet/outlet ports. Therefore, the optimized parameters were slightly modified to machine these layers without further optimization.

3.4. EMIS-based determination of resonance frequency

An impedance analyzer MFIA (Zurich Instrument, Zurich, Switzerland) was used to determine the resonance frequencies of the piezoelectric transducers and those of the microfluidic chips bonded with the same transducers (Fig. 5). A 12-$V_{p\text{-}p}$ sinusoidal signal in the frequency range of 1−10 kHz and a 2-$V_{p\text{-}p}$ sinusoidal signal in the frequency range of 10 kHz–1 MHz were applied to a device under test using a Kelvin clip lead (16089B, Keysight, Santa Rosa, CA, USA). The two different excitation voltages were used because the significant reduction in impedance at the higher frequency range caused a current overflow. The LabOne software (Zurich Instruments) was used to calibrate for the lead impedance, and to measure the magnitude $|\boldsymbol{Z}|$ and phase θ of the impedance as a function of frequency.

First, to evaluate the feasibility of our EMIS technique for identifying the resonance frequency f_r, a piezoelectric transducer (Murata 7BB-15−6L0) was tested as its f_r was known (6.0 ± 1.0 kHz). The transducer was not mechanically supported during the measurement to allow free bending. When the impedance was plotted on a log-log scale, resonance signatures (i.e., negative peak in $|\boldsymbol{Z}|$ and increasing shoulder in θ, as shown in Fig. 2c) appeared throughout the examined frequency band. Among the observed resonance signatures, the first resonance peak (i.e., the lowest flexural mode) was examined to determine whether its frequency was similar to the f_r of the transducer specification ($f_{r,Pf}$). Theoretical studies have been performed to formulate the mechanical resonance frequencies of a circular piezoelectric transducer, consisting of a PZT disc and a brass disc of a larger diameter [90,91]. However, a closed-form solution was not obtained. In another study, a closed-form

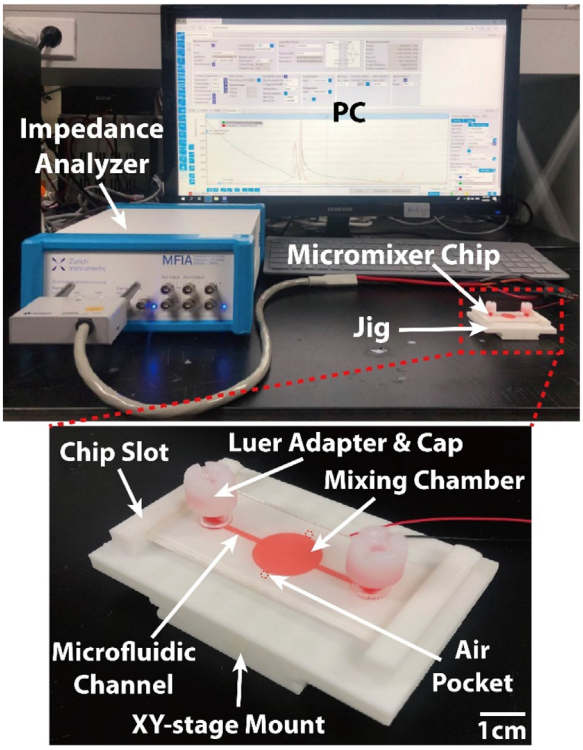

Fig. 5. EMIS (electromechanical impedance spectroscopy) setup. An impedance analyzer MFIA and the LabOne software (Zurich Instruments) were used for impedance measurements and resonance-frequency identification. The inset figure depicts an EMIS chip clamped with a custom 3D-printed jig. The inlet and outlet ports of the EMIS chip were capped to prevent water leakage during impedance measurement. Red food-coloring dye was used for visualization of the microchamber, two air bubbles, and microchannels.

solution for a transducer, which had equal PZT and brass diameters without edge support, was obtained [92]:

$$f_{r,Pf} = \frac{\lambda^2}{4\pi R^2}\sqrt{\frac{E_p^2 t_p^4 + E_b^2 t_b^4 + E_p E_b t_p t_b \left(2t_p^2 + 2t_b^2 + 3t_p t_b\right)}{3\left(E_p t_p + E_b t_b\right)\left(\rho_p t_p + \rho_b t_b\right)\left(1-\nu^2\right)}}, \quad (7)$$

where λ is the eigenvalue of the flexural mode, R is the radius of the discs, E is Young's modulus, t is the thickness, ρ is the density, and ν is the Poisson's ratio. The subscripts p and b correspond to the PZT and brass, respectively. Eq. (7) predicts a value of 5.46 kHz, which falls within the transducer specification. Resonance frequencies of higher flexural modes can be determined using a higher-order wavenumber λ (e.g., $\lambda = 6.2003$ for the 2nd axis-symmetric flexural mode) [93]. A radial-mode resonance frequency can be expressed as follows:

$$f_{r,Pr} = \frac{N_p}{d}, \quad (8)$$

where N_p is the planar acoustic wave velocity, and it was calculated to be on the order of 100 s kHz. The thickness mode resonance frequency can be expressed as follows:

$$f_{r,Pt} = \frac{N_t}{d}, \quad (9)$$

where N_t is the thickness acoustic wave velocity, and it was calculated to be on the order of 10 s MHz. The resonance frequencies of these modes are significantly higher than that of the fundamental (1 st) flexural mode [94,95] and even beyond the theoretical resonance frequency of an equivalent spherical bubble ($f_{r,Beq}$). Therefore, these frequencies were not considered for excitation.

After identifying the fundamental flexural mode of the piezoelectric transducer, we tested the microfluidic chip bonded with

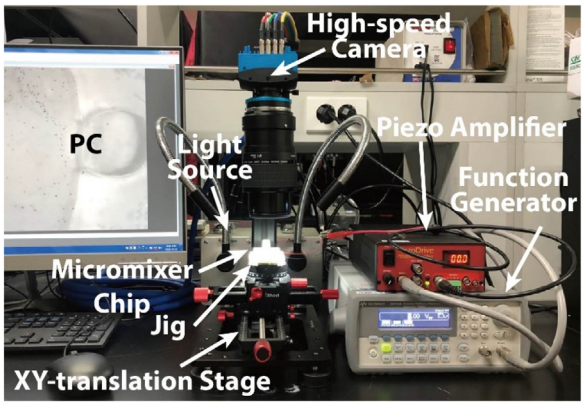

Fig. 6. Experimental setup for high-speed flow visualization. A high-speed camera equipped with a macro zoom lens (1×-5×) and LED light sources was used to capture streaming images at 180 fps. A function generator and a piezo amplifier were used to excite the micromixer chip with 60 V_{p-p} at each of four resonance frequencies. A custom XY-translational stage was also constructed to hold and move the chip for imaging.

the same transducer. As shown in the inset of Fig. 5, both chip edges were clamped using a custom jig fabricated using a 3D printer (Dimension 1200es, Stratasys, Rehovot, Israel). The jig had slots for the quick clamping and releasing of the microfluidic chips and a dovetail mount for easy coupling to our custom XY stage (see Section 3.5). The chip was filled with water, and the inlet and outlet Luer ports (#09–0512–0303–01, Microfluidic ChipShop, Jena, Germany) were tightly sealed with Luer plugs (#CP30033, iSUPPLY, Seongnam, Korea) to prevent leakage during impedance measurements. The flexural resonance frequency of a rectangular plate of length L, which is clamped at both ends, is expressed as follows [96]:

$$f_{r,Cf} = \frac{\lambda^2}{4\pi L^2}\sqrt{\frac{Et^2}{2\rho\left(1-\nu^2\right)}} \quad (10)$$

This equation predicts the resonance frequency of the fundamental flexural mode at 0.944 kHz, assuming a solid PMMA plate ($\lambda = 4.730$). As the chip was clamped lengthwise in the jig, the length-extensional vibration was interrupted and thus was not considered. The resonance frequency of the width-extension mode can be calculated as follows:

$$f_{r,Cw} = \frac{N_A}{w}, \quad (11)$$

where N_A is the acoustic wave velocity of PMMA, and w is the width of the chip. Eq. 11 predicts a resonance frequency of ~100 kHz, which is beyond the frequency range of interest. In contrast to the piezoelectric transducer, various mechanical losses, including viscous damping due to plate vibration, thermoelastic damping due to the bending of sandwiched plastic plates, and anchor loss in the slots, render the resonance signatures of the microfluidic chip indistinct and difficult to locate [58,63,95,97]. Regardless, the resonance signature of the lowest frequency, i.e., the 1 st flexural mode, was identified for excitation of the microfluidic chip ($f_{r,Cf}$) using the same principle that was employed to determine f_r of the piezoelectric transducer.

3.5. High-speed visualization and streaming pattern generation

In order to determine the effectiveness of cavitation microstreaming generated at different excitation frequencies and characterize the stability of vibrating bubbles trapped in air pockets of different shapes, we examined streaming patterns (i.e., pathlines). As illustrated in Fig. 6, our custom imaging setup

consists of a high-speed camera EoSens 4CXP (Mikrotron, Munich, Germany), which can capture up to 563 fps (frames per second) with a resolution of 2336 × 1728 pixels, connected to a PC through a CXP-6 interface (FireBird Quad, Active Silicon, Iver, UK). A macro zoom lens (MP—E 65 mm f/2.8 1×-5×, Canon, Tokyo, Japan) was used to capture streaming patterns around the air pockets of the EMIS chips. An XY-translational stage was custom-built by attaching a rotational Arca-Swiss quick-release plate (#IS-QJ58, iShoot, Shenzhen, China) to an XY macro focusing rail slider (#2xIS-MFR150, iShoot) installed on a vertical stand (#WVH01, Wemacro Rail, Shanghai, China). The high-speed camera was allowed to move in the z direction on a worm-drive macro rail (MFR-150S, Sunwayfoto, Zhongshan, China). The dovetail mount of the 3D-printed jig (Fig. 5, inset figure) facilitated coupling and decoupling of the microfluidic chips to the XY stage. Because the camera received small amounts of light at high frame rates, two LED gooseneck light sources (LED-50W, AmScope, Irvine, CA, USA) were used for illumination.

A 3-$V_{p\text{-}p}$ sinusoidal signal was generated using a function generator (33210A, Keysight) and amplified to 60 $V_{p\text{-}p}$ using a piezo amplifier (PD200, PiezoDrive, Newcastle, Australia) for excitation. A solution (0.025 vol.%) of 10-μm diameter black polystyrene microbeads (#24294–2, Polysciences, Warrington, PA, USA) was injected into the microchamber for seeding. The inlet/outlet ports were capped with the Luer-Lok plugs. The black microbeads in the background of white PMMA (the base layer) allow the capture of relatively high-contrast images. The motion of the microbeads induced by cavitation microstreaming was recorded at 180 fps for 4.45 s (total of 500 frames) with 2336 × 1728 resolution. Streaming patterns were obtained by synthesizing 100 frames (0.56 s) using ImageJ with the Flowtrace plugin.

Our high-speed imaging setup was also used to study the stability of bubbles trapped in air pockets of different shapes (Section 3.7). In addition, the mixing performance of the micromixer chips was evaluated using this setup (Section 3.8).

3.6. Experimental verification of the resonance frequencies

After all four resonance frequencies (i.e., $f_{r,B}$, the theoretical bubble resonance frequency assuming a perfect sphere; $f_{r,Beq}$, the theoretical bubble resonance frequency based on the equivalent sphere; $f_{r,Pf}$, the resonance frequency of a piezoelectric transducer based on the EMIS method; and $f_{r,Cf}$, the resonance frequency of the chip bonded with the transducer based on the EMIS technique) were identified, each frequency was evaluated by exciting the EMIS chip and examining the generated streaming patterns.

In a given excitation period, a faster the cavitation-microstreaming-induced circulatory flow corresponds to the longer and broader pathlines [48]. Thus, the length and range of the pathlines were qualitatively compared to determine which of the four resonance frequencies yielded the most effective mixing. In this way, the proposed method for determining excitation frequency was validated.

3.7. Determination of air-pocket shapes

After the proposed excitation-frequency determination method based on the EMIS technique and high-speed flow visualization was validated, the air-pocket shape of the micromixer chip was determined with consideration of enhancing mixing performance and device lifetime. As depicted in Fig. 3c, the micromixer chip had six air pockets on the perimeter of the microchamber for a wide coverage of circulatory streaming. During EMIS measurements, the bubbles inside the EMIS chip were stable (~4.5 min), as the excitation voltage was only 3–12 $V_{p\text{-}p}$. However, the bubble stability in the actual mixing experiments was insufficient because the 60-$V_{p\text{-}p}$ excitation induced far stronger vibration. Water rushed into the air pocket only after ~1.5 min of excitation. The bubble subsequently shrank inside the pocket, and the cavitation microstreaming faded, yielding weak circulatory flows. Chen et al. developed a model for the time-dependent changes in the bubble shapes in a rectangular pocket based on a pressure equilibrium across the air-water interface [48]. However, their model was based on the air permeability of PDMS and may not be applicable to the relatively air-impermeable PMMA used in this study. Therefore, we experimentally determined the pocket shapes that maximized the bubble stability.

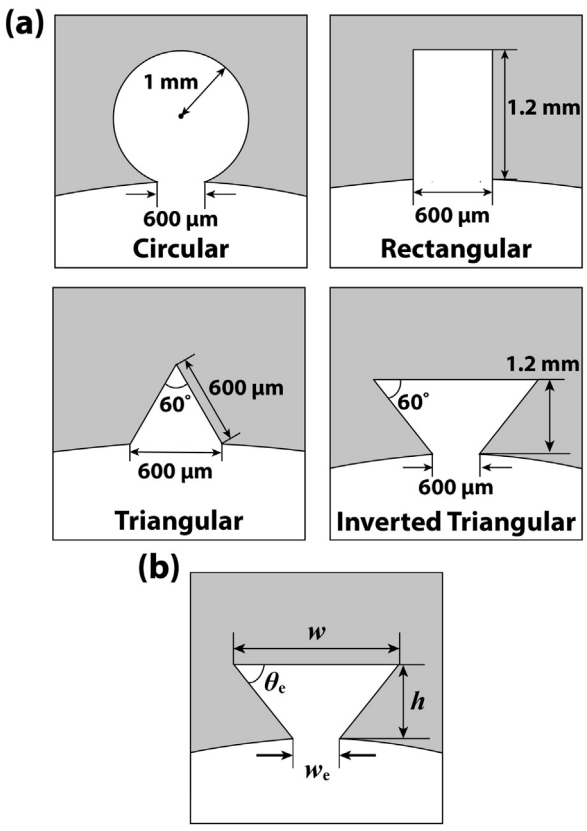

Fig. 7. Experimental determination of the air-pocket shape. (a) Schematics of the four different pocket designs for initial testing of the bubble stability (i.e., the EMIS chip). (b) Schematic of the inverted-triangular pocket with the entrance angle θ_e, the entrance width w_e, the height h, and the width w used for the micromixer chip.

As illustrated in Fig. 7, we tested various pocket designs: circular (2 mm in diameter), rectangular (0.6 mm × 1.2 mm), triangular (equilateral with a side length of 600 μm), and inverted-triangular shapes (height of 1.2 mm and entrance angle of 60°). The entrance width selected for all four shapes was 600 μm, because the bubbles were more stable than those trapped in circular air pockets with a 750-μm entrance width in our early EMIS chip design (Fig. 3b). Among these shapes, the inverted-triangular pockets exhibited the longest bubble lifetime (i.e., the average time before water started filling the air pocket). It was speculated that the sudden expansion of the cross section beyond the entrance acted as an interfacial energy barrier, extending the bubble lifetime [86,87]. The shape of the inverted triangle was modified by changing the entrance angle θ_e and width w_e (Fig. 7b). First, θ_e was varied: 35°, 40°, 60°, and 75° (base width w was varied accordingly) while w_e was fixed at 600 μm, and h was fixed at 1.2 mm. Both the bubble lifetime and the streaming patterns were characterized. The θ_e that maximized the lifetime was selected. Second, the entrance width w_e was varied (400, 600, 800, and 1000 μm) while θ_e was fixed at the optimal entrance angle, and the width w was fixed as 3 mm (height h was varied accordingly). The entrance width w_e that yielded the

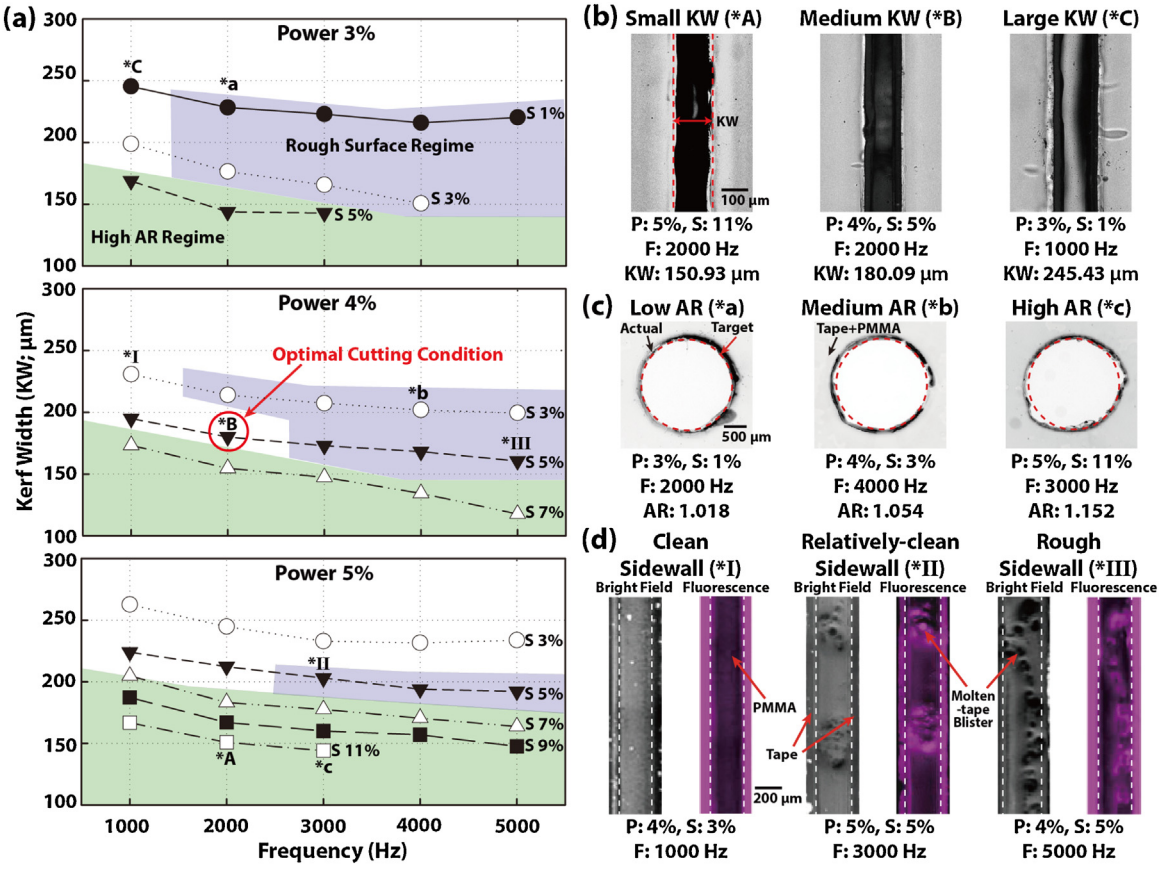

Fig. 8. Optimization of the laser-cutting parameters. (a) Kerf width (KW) is plotted with respect to P (power), S (speed), and F (frequency). The green area indicates the high-AR regime (unacceptable contour error), and the violet area indicates the rough-surface regime (unacceptable surface roughness). The red circle indicates the optimal cutting parameters satisfying the condition of the smallest KW with an acceptable contour error and surface roughness. The asterisked symbols (e.g., *A, *a, *I) indicate the exemplary cases for KW, AR, and roughness characterizations. (b) Partial images of 3-mm straight cuts for the three KW cases (small, medium, and large) are presented along with the corresponding cutting parameters and symbols. (c) Images of 2-mm-diameter circular cuts for the three AR cases (low, medium, and high) are highlighted along with the corresponding cutting parameters and symbols. (d) Bright-field and fluorescence images of the sidewalls of rectangular-cut samples for the three roughness cases (clean, relatively clean, rough) are depicted along with the corresponding cutting parameters and symbols. Strong fluorescence from tape and blisters and no fluorescence from non-blistered PMMA region suggested that the origin of the blisters is from the tape. The molten-tape blisters contributed to the surface roughness.

broadest streaming pattern and a reasonable lifetime (> 600 s) was selected. For both experiments, the lifetime was measured triplicate ($n = 3$). The selected w_e and θ_e were used in the design of the micromixer chip for actual mixing experiments.

3.8. Mixing-performance characterization

After the air-pocket design was completed, the mixing performance of the micromixer chip was evaluated. A macro lens (EF 50 mm f/2.5 compact macro, Canon) was used to observe the mixing phenomena in the entire microchamber over time. Deionized (DI) water and 75× diluted black ink (Sheaffer, Shelton, CT, USA) were co-injected into the microchamber through the inlet #1 and #2 using two syringe pumps Legato 200 (KD Scientific, Hollistion, MA, USA), which were equipped with a 3-mL syringe (HENKE-JECT 4020.X00V0, Henke-Sass Wolf, Tuttlingen, Germany), at a flow rate of 50 μL/min. Each liquid occupied approximately half of the microchamber. After the onset of the excitation, images of the entire microchamber were captured every 62.5 ms. Pixel intensity values of the individual chamber images were extracted using ImageJ to calculate mixing index (MI) as a function of time [7,46,98]:

$$\mathrm{MI} = 1 - \sqrt{\frac{1}{N}\sum_{i=1}^{N}\left(\frac{c_i - \bar{c}}{\bar{c}}\right)^2}, \qquad (10)$$

where c_i is the intensity of pixel i, and $\bar{c}$ is the average intensity over N pixels in the region of interest (i.e., the circular chamber). Because 8-bit grayscale images were obtained through our high-speed camera, the intensity value ranged from 0 to 255 (arbitrary unit). For the case of ideal 1:1 mixing, MI=∼0 corresponds to unmixed fluids, and MI=∼1 corresponds to completely homogenized fluids [98]. However, MI always converged to a value smaller than 1 after mixing is completed because of the inherent noise of the imaging system. We defined the mixing time as the time when MI reached 90 % of its steady-state value.

The mixing time was measured for three cases to confirm if the excitation frequency determined in Section 3.6 indeed yielded the most effective mixing: 1) excitation at the best resonance frequency, 2) excitation at the second-best resonance frequency, and 3) no excitation (i.e., negative control).

4. Results and discussion

4.1. Optimization of the laser-cutting parameters

As shown in Fig. 8a, the kerf width (KW) for the 3-mm straight cut (Fig. 4a) tended to decrease when the P (power) decreased, and S (speed) and F (frequency) increased. Fig. 8b presents exemplary images of the small-, medium-, and large-KW cases along with the corresponding cutting conditions. The composite tape-PMMA-tape sheet could not be penetrated for significantly small P and high S

combinations (e.g., P = 3% and S = 7, 9%; P = 4% and S = 9%) because of the decrease in the total transmitted energy (per unit length) [77]:

$$\text{Total transmitted energy} \propto \frac{P}{S} \quad (11)$$

The high aspect ratio (AR) regime (colored green) indicates that the cutting results for a target circle (2-mm diameter, Fig. 4b) were elliptical (AR > 1.06). As illustrated in Fig. 8c, the actual trajectory transformed from a circular shape to an oval shape as AR increased. Discontinuities in the elliptical trajectory were observed for AR = 1.152. We noted that AR tended to increase with S, which is well documented in motion-control-system researches [79]. No perceptible relationships between the other parameters (i.e., P and F) and the AR were observed.

The rough-surface regime (colored violet) signifies that the sidewall of a rectangular-cut sample (Fig. 4c) was rough, and that molten-tape blisters covered more than 20 % of the surface area. Fig. 8d shows three examples of surface roughness: clean, relatively clean, and rough. Fluorescence and bright-field images revealed that the area covered by the molten-tape blisters expanded as the roughness increased. The surface roughness tended to increase with an increase in S and a decrease in P. It was reported that the pulse overlap, which affects the microscopic smoothness of a cut surface, increases with increasing S and decreasing beam-spot diameter [77]. The beam-spot diameter increased with increasing P for CO_2-laser cutting of PMMA [99]. No noticeable relationship between the surface roughness and F was observed.

A cutting-parameter set (P, S, F) that yielded the smallest KW outside the rough-surface regime and high-AR regime was selected: P = 4%, S = 5%, and F = 2000 Hz (the solid red circle in Fig. 8a). The surface roughness was evaluated only outside the high-AR regime because the union of the high-AR regime and the rough-surface regime would not be considered in actual cutting experiments. The chamber layers for the EMIS chip and micromixer chip were cut using the optimized cutting parameters. For the 1-mm-thick top layer and 0.5-mm-thick base layer, identical values of S and F were maintained to ensure a similar contouring performance and surface roughness, but P was increased to cut through the thicker PMMA sheets. The selected cutting parameters for the top and base layers were P = 6%, S = 5%, and F = 2000 Hz.

4.2. EMIS determination of resonance frequency

The impedance spectrum of the piezoelectric transducer (Murata 7BB-15−6L0) is illustrated in Fig. 9a. A resonance signature (i.e., a positive resonance peak followed by a negative anti-resonance peak in the magnitude $|\boldsymbol{Z}|$ and a positive peak in the phase θ) for flexural vibration appeared at the lowest frequency of 5.86 kHz. The magnitude difference between resonance and anti-resonance was $\Delta|\boldsymbol{Z}|_{ra}$ = 25.7 kΩ, and the phase peak height was $\Delta\theta$ = 149.7°. A few higher flexural modes appeared at 17.15, 42.72, 68.68, and 107.9 kHz in the order of decreasing $\Delta|\boldsymbol{Z}|_{ra}$ and $\Delta\theta$. The ratios of the higher-mode frequencies to the fundamental frequency did not perfectly match the ratios of the theoretical values for a free circular plate [93]. This discrepancy could be attributed to the unequal radii of the PZT and brass plates (12 mm vs. 15 mm) and the asymmetry in the piezoelectric transducer (e.g., the axial misalignment of the PZT and brass plates, and the existence of soldered wires on one side of the disc) [90,92]. We observed another strong resonance signature at 178.34 kHz ($\Delta|\boldsymbol{Z}|_{ra}$ = 1.4 kΩ and $\Delta\theta$ = 165.2°) as well as its higher-order mode at 630.66 kHz. A weaker resonance signature at 167.20 kHz ($\Delta|\boldsymbol{Z}|_{ra}$ = 0.132 kΩ and $\Delta\theta$ = 45.3°) and its higher-order mode at 385.11 kHz also appeared. It was speculated that these resonance signatures could be attributed to the radial-mode vibration of the PZT, the brass disc, or the combined structure (i.e., piezoelectric unimorph), for which the calculated

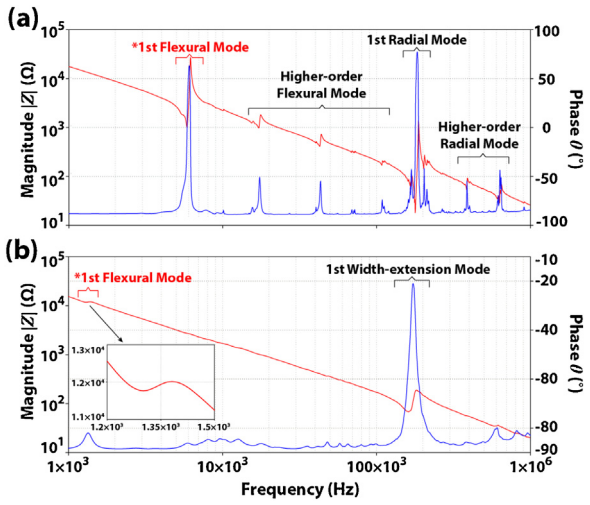

Fig. 9. Impedance plots for (a) the piezoelectric transducer and (b) the EMIS chip bonded with the transducer in the frequency range of 1 kHz–1 MHz. Various vibration modes characterized by resonant signatures (a negative resonance peak followed by a positive anti-resonance peak in the magnitude $|\boldsymbol{Z}|$ and a positive peak in the phase θ) are marked. The 1 st flexural mode marked by an asterisk (*) in both cases exhibited the strongest resonance signature (largest $\Delta|\boldsymbol{Z}|_{ra}$, i.e., the difference between the resonance and anti-resonance impedance in the magnitude). The inset figure displays less sharp resonance and anti-resonance peaks due to various mechanical losses that occurred in the oscillating microfluidic chip.

resonance frequencies were on the order of a few hundred kHz [95]. Because the maximum frequency of the impedance analyzer MFIA was 5 MHz, the thickness mode vibration could not be observed (calculated to be on the orders of 10 s MHz). The lowest flexural mode at 5.86 kHz exhibited the strongest resonance signature, as evidenced by the largest $\Delta|\boldsymbol{Z}|_{ra}$ value. A $\Delta|\boldsymbol{Z}|_{ra}$ value of the next-strongest resonance (i.e., the fundamental radial-mode resonance) was the 2nd largest. Consequently, 5.86 kHz was determined as $f_{r,Pf}$. The value of $f_{r,Pf}$ slightly varied (5.90 ± 0.03 kHz, n = 15), perhaps due to the manufacturing variation of the piezoelectric transducer.

The impedance spectrum of the EMIS chip bonded with the piezoelectric transducer is presented in Fig. 9b. Because of various losses in the oscillating mechanical structure, the resonance signatures were significantly less sharp than those of the transducer; the $\Delta|\boldsymbol{Z}|_{ra}$ and $\Delta\theta$ values are noticeably smaller [100]. A significant resonance signature was observed at 1.30 kHz with $\Delta|\boldsymbol{Z}|_{ra}$ = 247 Ω and $\Delta\theta$ = 6.5°. It was challenging to identify clear higher-order flexural modes; faint resonance signatures were observed at 4.76 and 5.75 kHz, but distinct resonance and anti-resonance peaks were not observed at these frequencies (i.e., $\Delta|\boldsymbol{Z}|_{ra}$=∼1 Ω and $\Delta\theta$=∼2°). These modes could be attributed to the flexural vibration of the micromixer chip [101] because the calculated fundamental resonance frequency for a clamped-clamped PMMA plate (i.e., a single block with no adhesive layers or no liquid) with the same dimensions was on the order of ∼1 kHz. Additionally, a strong resonance signature at 161.59 kHz ($\Delta|\boldsymbol{Z}|_{ra}$ = 119 Ω and $\Delta\theta$ = 66.1°) and faint higher-order modes at 580.13 and 599.18 kHz were identified ($\Delta|\boldsymbol{Z}|_{ra}$=∼1 Ω and $\Delta\theta$=∼5°). These vibrations may have originated from width-extension modes [83]. Because the flexural-vibration mode at 1.30 kHz exhibited the strongest resonance signature (the largest $\Delta|\boldsymbol{Z}|_{ra}$), its frequency was considered as $f_{r,Cf}$. The second-strongest resonance at 161.59 kHz was not considered because of a large temperature increase when the piezoelectric transducer was excited at this frequency. The value of $f_{r,Cf}$ also slightly varied (1.31 ± 0.04 kHz, n = 10) due to the chip-to-chip variations (e.g., machining error, misalignment between the chip layers, misalignment of the piezoelectric transducer with the

center of the chip, and asymmetry of the Luer-Lok adapter locations).

4.3. Experimental confirmation of the resonance frequency

Now that we have $f_{r,Cf}$ value obtained using the EMIS technique as well as $f_{r,Beq}$ value calculated using the concept of the equivalent spherical bubble, we sought to verify these resonance frequencies by exciting an EMIS chip and analyzing the resulting streaming patterns. The EMIS chip was excited at the four different frequencies ($f_{r,Cf}$ = 1.30 kHz, $f_{r,B}$ = 3.78 kHz, $f_{r,Pf}$ = 5.86 kHz, and $f_{r,Beq}$ = 26.82 kHz). $f_{r,Pf}$ was measured for a PZT transducer. Then, $f_{r,Cf}$ of a chip was measured after bonding with that transducer. $f_{r,B}$ was calculated using the radius of curvature R_o of the air-water interface of a bubble (Fig. 1b) after the seeded solution was loaded into the chamber. Lastly, $f_{r,Beq}$ was calculated using the equivalent bubble radius R_{eq} obtained with R_o, θ, and h (Fig. 1c).

Fig. 10 illustrates the streaming patterns generated from an oscillating bubble trapped in the top circular air pocket of an EMIS chip for a period of 0.56 s. Overall, the streaming pattern generated at $f_{r,Cf}$ (Fig. 10a) denotes the longest and broadest pathlines. We also observed the largest flexural vibration of the EMIS chip during this excitation. The results confirm our hypothesis that the maximum structural vibration can generate the largest air-water interface oscillation, thereby producing the most effective cavitation microstreaming. Thereafter, $f_{r,Cf}$ of an individual micromixer chip was measured using the EMIS method, and its resonance frequency was used for excitation in mixing experiments.

The second-best resonance frequency was $f_{r,Beq}$ (Fig. 10d). Although the streaming pattern exhibited relatively long pathlines (i.e., a fast flow), the pattern was confined within the vicinity of the air-water interface. The air-water interface became quickly unstable at this resonance frequency. The air leaked out and formed bubbles that randomly adhered to the chamber sidewall. Streaming emanated from these sporadically trapped bubbles. The worst-performing resonance frequency was $f_{r,B}$ (Fig. 10c), which was based on the perfect freestanding sphere assumption and the Rayleigh-Plesset equation (Eq. (3)). These results indicate that our approach based on the concept of the equivalent spherical bubble and the Rayleigh-Plesset equation is more accurate than the traditional approach, wherein a perfect sphere was assumed. The third-best resonance frequency was $f_{r,Pf}$ (Fig. 10b), which can be explained by the difference in vibration dynamics between the piezoelectric transducer and the chip bonded with the transducer.

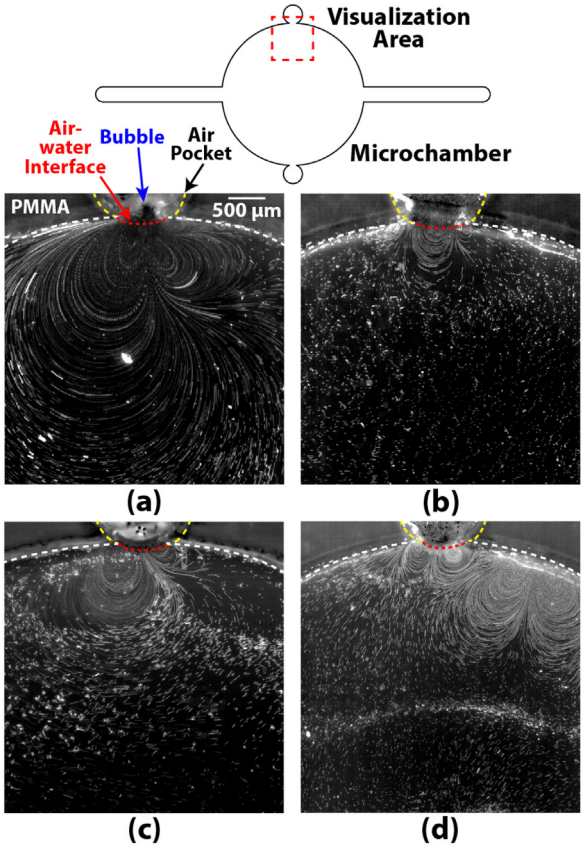

Fig. 10. Streaming patterns generated by a vibrating bubble trapped in the top circular air pocket of an EMIS chip (top panel). The chip was excited at (a) 1.30 kHz, the chip resonance frequency based on the EMIS method ($f_{r,Cf}$), (b) 3.78 kHz, the theoretical bubble resonance frequency assuming a perfect sphere ($f_{r,B}$), (c) 5.86 kHz, the piezoelectric transducer resonance frequency based on the EMIS method ($f_{r,Pf}$), and (d) 26.8 kHz, the theoretical bubble resonance frequency based on an equivalent sphere with the area same as the air-water interface area ($f_{r,Beq}$).

4.4. Determination of air-pocket shapes

It was experimentally proved that, $f_{r,Cf}$, the chip resonance frequency measured using the EMIS method indeed exhibited the most effective cavitation microstreaming among the other frequen-

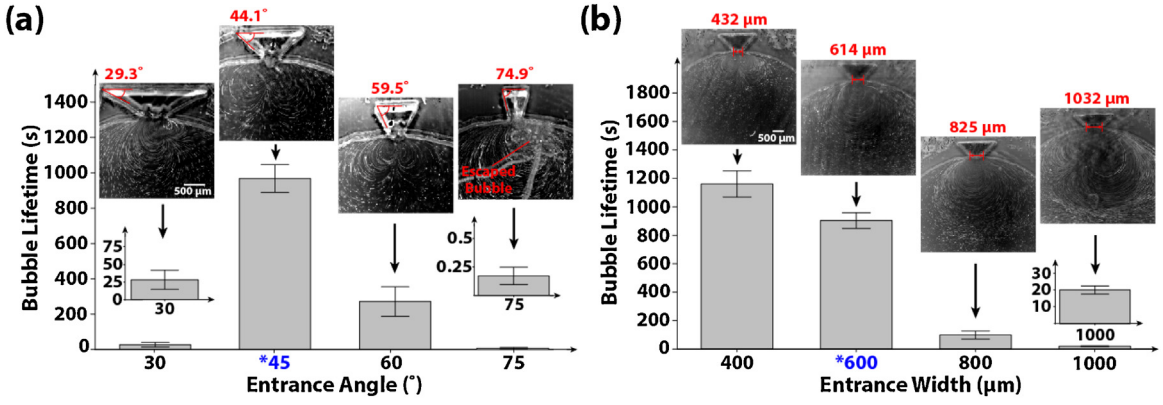

Fig. 11. Determination of the shape of inverted triangular air pockets. (a) The bubble lifetime was measured when the entrance angle θ_e was increased from 30° to 75°, and the entrance width w_e was fixed at 600 μm. The measured angle is shown in red, and the abscissa of the graph indicates the nominal angle. Streaming patterns were synthesized with 100 consecutive images. Air initially trapped in the air pocket escaped and formed an oscillating bubble outside of the pocket for the 75° case. (b) The bubble lifetime was measured when the entrance width w_e varied from 400 to 1000 μm, and the entrance angle θ_e was fixed at the value of 45° from (a). The corresponding streaming patterns indicate that the area covered by circulatory flows expanded as w_e increased. Note: magnification for figures in (b) is smaller than that for figures in (a) because the pathlines for (b) cover broader areas.

cies tested. Next, we designed air pockets of a micromixer chip for a prolonged bubble lifetime and excellent mixing performance.

First, the entrance angle θ_e of the inverted-triangular air pockets was increased from 30° to 75° while the entrance width w_e was maintained at 600 μm, and based width w was varied accordingly (Fig. 11a). The lifetime was unusably short at 30° (28 s). Then, the lifetime was maximized at 45° (968 s), and it decreased sharply as θ_e increased further. At 75°, the bubbles in the air pocket collapsed, and the air escaped almost instantaneously (0.67 s). Consequently, 45° was selected as the entrance angle θ_e.

Second, the entrance width w_e varied from 400 to 1000 μm with the best θ_e (=45°) while w was fixed at 3 mm, and h was adjusted accordingly. The pathlines were progressively extended and expanded, indicating that cavitation microstreaming became more effective as the entrance width increased (Fig. 11b). However, the lifetime of the bubbles monotonically decreased from 1160 to 21 s as w_e increased. At 600 μm, the bubble lifetime was reasonable (904 s), which was more than the targeted lifetime of 600 s, and reasonably wide and fast cavitation microstreaming was observed. Therefore, 600 μm was selected as the entrance width w_e. The width of the streaming pattern from the w_e = 600 μm case was approximately 6.1 mm (Fig. 11b), which is ~41 % of the chamber diameter. Therefore, more than two of these air pockets were required on the chamber to maximize the area swept by cavitation microstreaming (Fig. 3c). In summary, an entrance angle of 45°and entrance width of 600 μm were used to design the inverted triangular air pockets for the micromixer chip.

4.5. Mixing-performance characterization

Micromixer chips with six-inverted triangular air pockets were fabricated (Fig. 3c). The flexural resonance frequency $f_{r,Cf}$ of each chip was individually measured using the EMIS method before conducting mixing experiments. It was challenging to fill exactly half of the chamber with each liquid (diluted ink through Inlet #1 and DI water through Inlet #2) due to slight asymmetry in the tubing and inlet channel lengths. However, approximately half of the microchamber was filled with each liquid by carefully adjusting both injection flow rates (see inset figures for 0 s in Fig. 12). For the three experimental cases (i.e., $f_{r,Cf}$, $f_{r,Beq}$, and negative control), mixing was performed for ~300 s, but the images were collected for only 138 s owing to the memory limit.

As seen in Fig. 12a, the mixing time, at which MI reached 90 % of its steady-state value (0.931), was 37.2 s when the mixer was excited at $f_{r,Cf}$. During the mixing time, the six air bubbles were intact (no bubble escaped) thanks to the optimized pocket design. The mixing time was worse (>300 s) for excitation at the second-best resonance frequency $f_{r,Beq}$. MI was only 0.147 at 37.2 s (i.e., the mixing time for the $f_{r,Cf}$ case). Furthermore, bubbles were not stable at $f_{r,Beq}$ because bubbles started escaping from the air pockets after ~36 s. MI for the negative control (no excitation) reached only 0.085 even after 138 s as diffusion was only mass-transport mechanism. Consequently, we experimentally confirmed that exciting the micromixer chip at its flexural resonance frequency, measured via the EMIS technique, offers the most effective mixing. The EMIS technique is a general method of determining the resonance frequency. Therefore, it could be applied to any micromixer equipped with a piezoelectric transducer.

The mixing time we achieved here may not appear impressive when compared with the values presented in the literature [1,7,13]. However, R_{sv}, the ratio between active surface area (e.g., a moving portion of liquid boundary) and mixing volume, should be considered when evaluating mixing time because it would take longer to mix a large volume of liquid with a small active surface area. For example, a previous cavitation micromixer of a similar design yielded a mixing time of 6 s because its R_{sv} value was 133 (i.e., 35 air

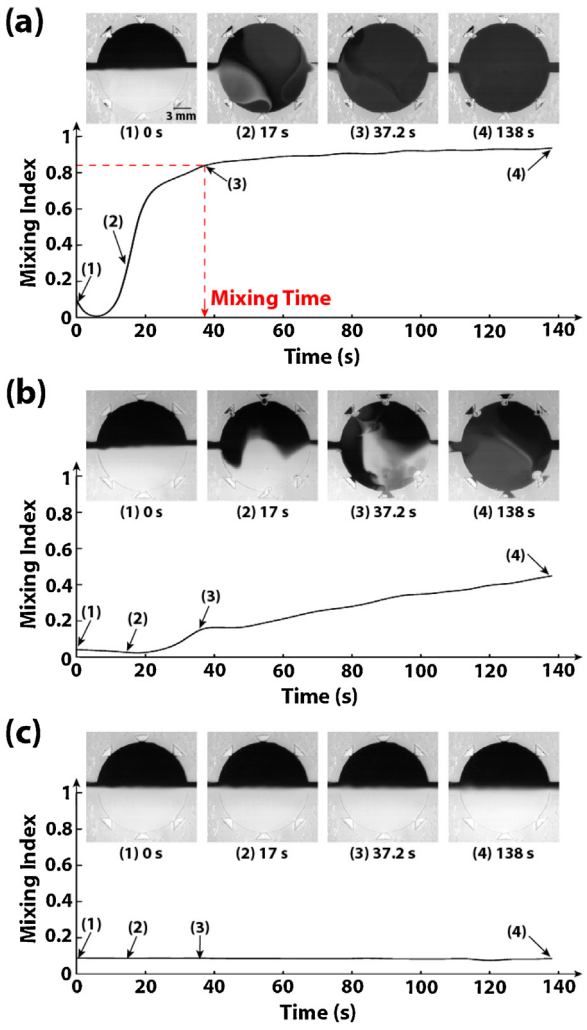

Fig. 12. MI (mixing index)-based performance characterization of a micromixer chip integrated with the inverted-triangular air pockets of the optimized shape. Inset figures show grayscale images of the mixing chamber over time. (a) The micromixer chip was excited at the fundamental flexural resonance frequency ($f_{r,Cf}$). Mixing time, defined as the time when MI reached 90 % of its steady-state value, was 37.2 s. (b) The mixer was excited at the second-best frequency ($f_{r,Beq}$), which is the theoretical resonance frequency based on the equivalent bubble. The bubble started escaping the pockets after 36 s. The MI value was only 0.147 at 37.2 s. (c) The chip was not excited (negative control). Practically no mixing was observed during 138 s.

pockets of 500 μm diameter for mixing 16 × 16 × 0.2 mm^3 volume) [51]. The R_{sv} value of our mixer is only 20, indicating a relatively larger volume to homogenize. As the method of determining excitation frequency has been successfully developed, mixing time could be improved significantly by having a micromixer design with a larger R_{sv} value in the future.

5. Conclusion

The cavitation-microstreaming micromixer has caught attention because of its simple microfabrication, straightforward operation, relative insensitivity to experimental conditions, and exceptionally rapid mixing. Therefore, it has been employed for various biological and biochemical applications. However, in previous studies, excitation frequency, the critical operating condition for effective mixing, was determined according to an incomplete mathematical expression or an inaccurate assumption that the trapped bubbles are spherical, both of which would lead to mediocre mixing performance. In some cases, the excitation fre-

quency was empirically determined via an exhaustive search over a frequency band, which is time-consuming.

The EMIS technique has been extensively used for studying the oscillatory behaviors of mechanical structures because of the strong electromechanical coupling between a structure and a bonded piezoelectric transducer. Here we propose to use the EMIS technique in a systematic manner to determine the flexural resonance frequency of the micromixer chip, which is indeed a mechanical structure. The EMIS-based resonance-frequency detection was rapid (~4.5 min) and accurate, as confirmed by the streaming patterns generated by bubbles oscillating at these identified resonance frequencies.

The laser microfabrication process of PMMA based on the double-sided tape was experimentally optimized with regard to machining resolution (KW of ~200 μm), contouring performance (AR < 1.06), and surface smoothness. Our cleanroom-free microfabrication method was rapid (~10 min from CAD design to a completely assembled chip) and did not require the alignment of adhesive layers with a structural layer between them.

Our micromixer, which has air pockets designed for a maximum bubble lifetime and a broad mixing coverage, was excited at the individually measured flexural resonance frequency. Considering an ample mixing volume (61.9 μL), the micromixer exhibited promising mixing performance (mixing time of 37.2 s). During the mixing, air bubbles were stable inside the air pockets. We expect that our micromixer, having an optimized operational condition, straightforward fabrication, and excellent performance, will be adopted in many microfluidic applications in the near future. We are currently developing a DNA-extraction microdevice based on our EMIS method and laser-microfabrication process [102].

CRediT authorship contribution statement

Hyunjin Jeon: Investigation, Visualization, Data curation, Formal analysis, Validation. **Kaba Abdi Mirgissa:** Investigation, Methodology. **Seonhyuk Baek:** Investigation, Methodology. **Kyehan Rhee:** Conceptualization, Validation. **Dohyun Kim:** Writing - original draft, Writing - review & editing, Formal analysis, Conceptualization, Methodology, Supervision, Project administration, Funding acquisition, Validation.

Declaration of Competing Interest

The authors declare no conflict of interest.

Acknowledgements

This work (Grants No. S2601365) was supported by project for Cooperative R&D between Industry, Academy, and Research Institute funded by the Korea Ministry of SME and Startups in 2018. This work was also supported by the Korea Institute of Energy Technology Evaluation and Planning (KETEP) and the Ministry of Trade, Industry & Energy (MOTIE) of the Republic of Korea (No. 20174010201160).

Appendix A

Device design

The top layer was made of 1-mm-thick transparent PMMA and had inlet and outlet holes (2 mm diameter) for attaching female Luer-Lok ports for the facile coupling of tubes.

The chamber layer was made of 250-μm-thick transparent PMMA, having a central mixing chamber (15 mm diameter) and microchannels connecting the inlet and outlet holes to the chamber. For the EMIS chip, two circular air pockets (2 mm in diameter) are situated at the top and bottom of the chamber for unobstructed observation of streaming patterns from trapped bubbles (Fig. 3b). The entrance width of the air pocket was chosen as 750 μm after noticing that wider entrance widths (e.g., 1 mm) resulted in instant flooding upon agitation. The entrance width was later reduced (600 μm) for a longer bubble lifetime and wider microstreaming coverage (see Section 4.4). The microchannel dimensions were 12.5 mm × 1.6 mm. The 12.5-mm channel length was determined considering the size of the microchamber, a sufficient distance from the chip edge to the inlet/outlet ports (~10 mm), and enough clearance from the Luer-Lok ports (7.8-mm diameter and 9.14 mm height) for microscope imaging. The 1.6-mm channel width was chosen for easy liquid loading (i.e., negligible hydrodynamic resistance). Circular, rectangular, triangular, and inverted-triangular shapes with different dimensions were tested for the optimization of the air-pocket shape. The shape of

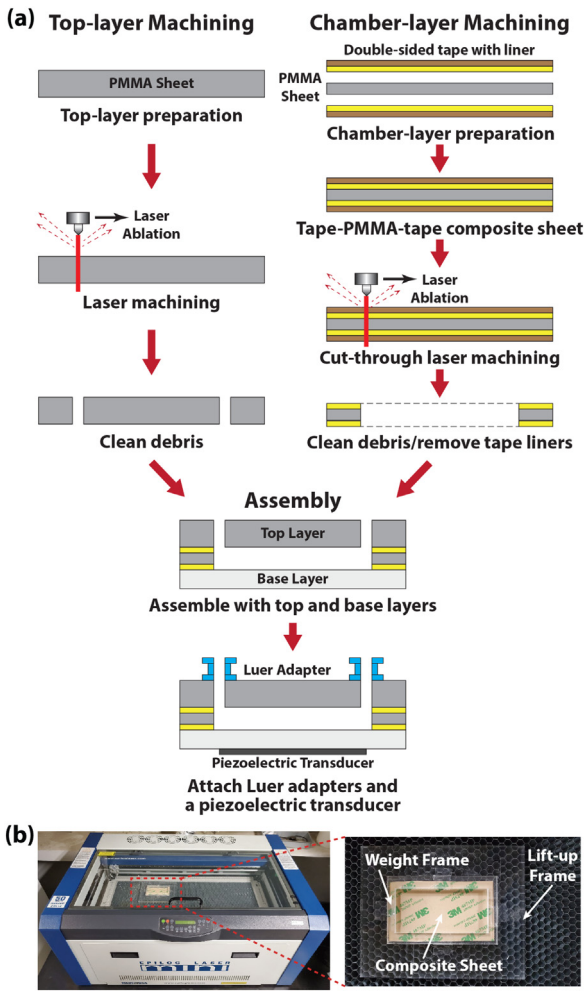

Fig. A1. (a) Proposed tape-assisted laser microfabrication process. A 1-mm-thick PMMA sheet was machined to form the top layer with inlet/outlet ports. Double-sided tapes, wherein one of the liners was removed, were pre-pasted to a 250-μm PMMA sheet to form a tape-PMMA-tape composite sheet. The 570-μm-thick composite sheet was cut through to form the chamber layer with microfluidic features using optimized laser-cutting parameters. The chamber layer was securely bonded between the top layer and the base layer (500-μm-thick white PMMA) using an artist roller after laser-ablation debris were cleaned, and the remaining liners were removed. The fabrication process was completed by bonding a piezoelectric transducer on the base layer and Luer-Lok fluidic adapters to the top layer. (b) Laser-machining setup based on an Epilog Mini 24 laser cutter. A custom-made PMMA frame set was used to lift the composite sheet from the honeycomb grid to avoid burning marks.

the air pocket yielding the maximum stability and effectiveness of the cavitation microstreaming was experimentally determined (see Section 3.7 for further detail). For the micromixer chip, six inverted-triangular air pockets were placed along the microchamber perimeter (Fig. 3c). The angle between two neighboring pockets was 45°. The entrance angle (i.e., the base angles of the inverted triangle) was θ_e, and the entrance width was w_e. The height and base width of the triangle were denoted as h and w, respectively. Two inlet ports (inlets #1 and #2) were used to bring two different liquids, diluted ink and deionized (DI) water, into the chamber for mixing. Two input microchannels (14.85 mm × 1.6 mm) from the inlet ports merged to be connected to the mixing chamber. An output microchannel (12.5 mm × 1.6 mm) connected the mixing chamber to the outlet port.

The base layer was made of 500-μm-thick white PMMA. The white color was selected so that the strong yellowish color of the brass plate of the piezoelectric transducer in the background was screened, and polystyrene tracer microbeads were clearly observed for streaming pattern visualization.

Microfabrication

The fabrication process is summarized in Fig. A1a. A CO_2 laser machine Mini 24 (Epilog, Golden, CO, USA; Fig. A1b) was used to cut PMMA (polymethyl methacrylate) sheets using optimized cutting parameters P (power), S (speed), and F (frequency). All the PMMA sheets were thoroughly cleaned before the machining.

First, a 1-mm-thick transparent PMMA (Acryl-Choiga, Seoul, Korea) was machined to form the outline and two fluidic ports of the top layer. Laser-ablation debris on the PMMA piece was removed by using a compressed nitrogen gun.

Second, after peeling off one of the two tape liners (16-μm thick), pressure-sensitive double-sided tape 467MP-200MP (33-μm-thick adhesive; 3 M, Saint Paul, MN, USA) was pre-pasted to both sides of a 250-μm-thick transparent PMMA sheet (Goodfellow, Huntingdon, UK) to form a composite sheet. Subsequently, the composite sheet (total thickness of 570 μm) was placed on a custom-made PMMA frame set. One frame (152 mm × 123 mm) was used for lifting the composite sheet from the honeycomb grid, and the other (115 mm × 115 mm) was used for weighing the sheet down, as depicted in Fig. A1b. The composite sheet was cut through by laser ablation to pattern the chamber layer with microfluidic features. By placing the composite sheet on the lift-up frame, burning marks due to the underlying honeycomb grid were avoided. After removing ablation debris, the remaining two liners were peeled off the chamber layer to expose the adhesives. By ablating through a tape-PMMA-tape composite sheet, the cut patterns in the adhesives and PMMA were self-aligned. Therefore, a time-consuming alignment between the adhesives and the patterned PMMA sheet was not necessary.

Lastly, a white PMMA sheet (500-μm thick; Hesa-Glas, Sydney, Australia) was machined to form the base layer. The top and base layers were carefully aligned and bonded to the chamber layer via both exposed adhesives. Then, an artist roller was used to apply pressure and squeeze out the bubbles trapped during the initial bonding. The alignments between the top and chamber layers and the base and chamber layers had a large tolerance; the inlet/outlet ports were larger than the channel width (2 mm vs. 1.6 mm, respectively), and the base layer did not have any features to align. A piezoelectric unimorph transducer, called a disc bender (7BB-15–6L0, Murata, Kyoto, Japan), consisting of a PZT disc and a circular brass plate, was bonded to the bottom of the assembled chip by applying super glue (AD127, 3 M) evenly with a brush. The disc bender was chosen because it is affordable (~$0.80 per piece), and the brass plate provides mechanical supports during handling or attaching to the chip. Finally, after being centered on the fluidic ports, two female Luer-Lok compatible adapters (Microfluidic ChipShop) were bonded to the top layer by using the same super glue to complete the fabrication process.

References

[1] G.S. Jeong, S. Chung, C.-B. Kim, S.-H. Lee, Applications of micromixing technology, Analyst 135 (2010) 460–473.
[2] L.J. Lucas, J.-H. Han, J.-Y. Yoon, Using highly carboxylated microspheres to simplify immunoassays and enhance diffusional mixing in a microfluidic device, Colloids Surf. B Biointerfaces 49 (2006) 106–111.
[3] X. Wang, X. Chen, X. Ma, X. Kong, Z. Xu, J. Wang, Fast DNA hybridization on a microfluidic mixing device based on pneumatic driving, Talanta 84 (2011) 565–571.
[4] J. Lee, H.K. Musyimi, S.A. Soper, K.K. Murray, Development of an automated digestion and droplet deposition microfluidic chip for MALDI-TOF MS, J. Am. Soc. Mass Spectrom. 19 (2011) 964–972.
[5] P.W. Miller, Radiolabelling with short-lived PET (positron emission tomography) isotopes using microfluidic reactors, J. Chem. Technol. Biotechnol. 84 (2009) 309–315.
[6] D.J. Beebe, G.A. Mensing, G.M. Walker, Physics and applications of microfluidics in biology, Annu. Rev. Biomed. Eng. 4 (2002) 261–286.
[7] G. Cai, L. Xue, H. Zhang, J. Lin, A review on micromixers, Micromachines 8 (2017) 274.
[8] K. Ward, Z.H. Fan, Mixing in microfluidic devices and enhancement methods, J. Micromech. Microeng. 25 (2015), 094001.
[9] L. Capretto, W. Cheng, M. Hill, X. Zhang, Micromixing within microfluidic devices, in: B. Lin (Ed.), Microfluidics Technologies and Applications, Springer, Heidelberg, 2011, pp. 27–68.
[10] N.-T. Nguyen, Z. Wu, Micromixers—a review, J. Micromech. Microeng. 15 (2004) R1.
[11] Y.K. Suh, S. Kang, A review on mixing in microfluidics, Micromachines 1 (2010) 82–111.
[12] N.-T. Nguyen, Mixing in microscale, in: S. Hardt, F. Schönfeld (Eds.), Microfluidic Technologies for Miniaturized Analysis Systems, Springer, Boston, 2007, pp. 117–155.
[13] C.-Y. Lee, C.-L. Chang, Y.-N. Wang, L.-M. Fu, Microfluidic mixing: a review, Int. J. Mol. Sci. 12 (2011).
[14] J.M. Ottino, S. Wiggins, Introduction: mixing in microfluidics, Philos. Trans. R. Soc. London, Ser. A (2004) 923–935.
[15] C.-Y. Lee, W.-T. Wang, C.-C. Liu, L.-M. Fu, Passive mixers in microfluidic systems: a review, Chem. Eng. J. 288 (2016) 146–160.
[16] V. Hessel, H. Löwe, F. Schönfeld, Micromixers—a review on passive and active mixing principles, Chem. Eng. Sci. 60 (2005) 2479–2501.
[17] S. Hardt, K. Drese, V. Hessel, F. Schönfeld, Passive micromixers for applications in the microreactor and μTAS fields, Microfluid. Nanofluid. 1 (2005) 108–118.
[18] D.S. Kim, S.W. Lee, T.H. Kwon, S.S. Lee, A barrier embedded chaotic micromixer, J. Micromech. Microeng. 14 (2004) 798.
[19] Y. Lin, G.J. Gerfen, D.L. Rousseau, S.-R. Yeh, Ultrafast microfluidic mixer and freeze-quenching device, Anal. Chem. 75 (2003) 5381–5386.
[20] A.D. Stroock, S.K. Dertinger, A. Ajdari, I. Mezić, H.A. Stone, G.M. Whitesides, Chaotic mixer for microchannels, Science 295 (2002) 647–651.
[21] J.-T. Yang, K.-J. Huang, K.-Y. Tung, I.-C. Hu, P.-C. Lyu, A chaotic micromixer modulated by constructive vortex agitation, J. Micromech. Microeng. 17 (2007) 2084.
[22] A.-S. Yang, F.-C. Chuang, C.-K. Chen, M.-H. Lee, S.-W. Chen, T.-L. Su, Y.-C. Yang, A high-performance micromixer using three-dimensional Tesla structures for bio-applications, Chem. Eng. J. 263 (2015) 444–451.
[23] T.W. Lim, Y. Son, Y.J. Jeong, D.-Y. Yang, H.-J. Kong, K.-S. Lee, D.-P. Kim, Three-dimensionally crossing manifold micro-mixer for fast mixing in a short channel length, Lab Chip 11 (2011) 100–103.
[24] C.-P. Jen, C.-Y. Wu, Y.-C. Lin, C.-Y. Wu, Design and simulation of the micromixer with chaotic advection in twisted microchannels, Lab Chip 3 (2003) 77–81.
[25] T.J. Ober, D. Foresti, J.A. Lewis, Active mixing of complex fluids at the microscale, Proc. Natl. Acad. Sci. U.S.A. 112 (2015) 12293–12298.
[26] L.-H. Lu, K.S. Ryu, C. Liu, A magnetic microstirrer and array for microfluidic mixing, J. Microelectromech. Syst. 11 (2002) 462–469.
[27] S.H. Lee, D. van Noort, J.Y. Lee, B.-T. Zhang, T.H. Park, Effective mixing in a microfluidic chip using magnetic particles, Lab Chip 9 (2009) 479–482.
[28] T. Frommelt, M. Kostur, M. Wenzel-Schäfer, P. Talkner, P. Hänggi, A. Wixforth, Microfluidic mixing via acoustically driven chaotic advection, Phys. Rev. Lett. 100 (2008), 034502.
[29] S.Y. Tang, V. Sivan, P. Petersen, W. Zhang, P.D. Morrison, K. Kalantar-zadeh, A. Mitchell, K. Khoshmanesh, Liquid metal actuator for inducing chaotic advection, Adv. Funct. Mater. 24 (2014) 5851–5858.
[30] J.-H. Tsai, L. Lin, Active microfluidic mixer and gas bubble filter driven by thermal bubble micropump, Sens. Actuators A Phys. 97 (2002) 665–671.
[31] W.Y. Ng, S. Goh, Y.C. Lam, C. Yang, I. Rodríguez, DC-biased AC-electroosmotic and AC-electrothermal flow mixing in microchannels, Lab Chip 9 (2009) 802–809.
[32] J. Kim, M. Johnson, P. Hill, B.K. Gale, Microfluidic sample preparation: cell lysis and nucleic acid purification, Integr. Biol. 1 (2009) 574–586.

[33] M. Wiklund, R. Green, M. Ohlin, Acoustofluidics 14: applications of acoustic streaming in microfluidic devices, Lab Chip 12 (2012) 2438–2451.
[34] W. Cui, W. Pang, Y. Yang, T. Li, X. Duan, Theoretical and experimental characterizations of gigahertz acoustic streaming in microscale fluids, Nanotechnol. Prec. Eng. 2 (2019) 15–22.
[35] Z. Yang, S. Matsumoto, H. Goto, M. Matsumoto, R. Maeda, Ultrasonic micromixer for microfluidic systems, Sens. Actuators A Phys. 93 (2001) 266–272.
[36] M. Bengtsson, T. Laurell, Ultrasonic agitation in microchannels, Anal. Bioanal. Chem. 378 (2004) 1716–1721.
[37] R.H. Liu, J. Yang, M.Z. Pindera, M. Athavale, P. Grodzinski, Bubble-induced acoustic micromixing, Lab Chip 2 (2002) 151–157.
[38] A. Hashmi, G. Yu, M. Reilly-Collette, G. Heiman, J. Xu, Oscillating bubbles: a versatile tool for lab on a chip applications, Lab Chip 12 (2012) 4216–4227.
[39] S.O. Catarino, L.R. Silva, P. Mendes, J. Miranda, S. Lanceros-Mendez, G. Minas, Piezoelectric actuators for acoustic mixing in microfluidic devices—numerical prediction and experimental validation of heat and mass transport, Sens. Actuators B Chem. 205 (2014) 206–214.
[40] A. Sonato, M. Agostini, G. Ruffato, E. Gazzola, D. Liuni, G. Greco, M. Travagliati, M. Cecchini, F. Romanato, A surface acoustic wave (SAW)-enhanced grating-coupling phase-interrogation surface plasmon resonance (SPR) microfluidic biosensor, Lab Chip 16 (2016) 1224–1233.
[41] G.G. Yaralioglu, I.O. Wygant, T.C. Marentis, B.T. Khuri-Yakub, Ultrasonic mixing in microfluidic channels using integrated transducers, Anal. Chem. 76 (2004) 3694–3698.
[42] D. Ahmed, X. Mao, J. Shi, B.K. Juluri, T.J. Huang, A millisecond micromixer via single-bubble-based acoustic streaming, Lab Chip 9 (2009) 2738–2741.
[43] Z. Yang, H. Goto, M. Matsumoto, R. Maeda, Active micromixer for microfluidic systems using lead-zirconate-titanate (PZT)-generated ultrasonic vibration, Electrophoresis 21 (2000) 116–119.
[44] C.E. Brennen, Cavitation and Bubble Dynamics, Cambridge University Press, 2014.
[45] P. Tho, R. Manasseh, A. Ooi, Cavitation microstreaming patterns in single and multiple bubble systems, J. Fluid Mech. 576 (2007) 191–233.
[46] A. Ozcelik, D. Ahmed, Y. Xie, N. Nama, Z. Qu, A.A. Nawaz, T.J. Huang, An acoustofluidic micromixer via bubble inception and cavitation from microchannel sidewalls, Anal. Chem. 86 (2014) 5083–5088.
[47] S.S. Wang, Z.J. Jiao, X.Y. Huang, C. Yang, N.T. Nguyen, Acoustically induced bubbles in a microfluidic channel for mixing enhancement, Microfluid. Nanofluid. 6 (2009) 847–852.
[48] H. Chen, Y. Gao, K. Petkovic, S. Yan, M. Best, Y. Du, Y. Zhu, Reproducible bubble-induced acoustic microstreaming for bead disaggregation and immunoassay in microfluidics, Microfluid. Nanofluid. 21 (2017) 30.
[49] A.R. Tovar, A.P. Lee, Lateral cavity acoustic transducer, Lab Chip 9 (2009) 41–43.
[50] D. Ahmed, X. Mao, B.K. Juluri, T.J. Huang, A fast microfluidic mixer based on acoustically driven sidewall-trapped microbubbles, Microfluid. Nanofluid. 7 (2009) 727.
[51] R.H. Liu, R. Lenigk, R.L. Druyor-Sanchez, J. Yang, P. Grodzinski, Hybridization enhancement using cavitation microstreaming, Anal. Chem. 75 (2003) 1911–1917.
[52] Y. Okabe, Y. Chen, R. Purohit, R.M. Corn, A.P. Lee, Piezoelectrically driven vertical cavity acoustic transducers for the convective transport and rapid detection of DNA and protein binding to DNA microarrays with SPR imaging—a parametric study, Biosens. Bioelectron. 35 (2012) 37–43.
[53] A. De Vellis, D. Gritsenko, Y. Lin, Z. Wu, X. Zhang, Y. Pan, W. Xue, J. Xu, Drastic sensing enhancement using acoustic bubbles for surface-based microfluidic sensors, Sens. Actuators B Chem. 243 (2017) 298–302.
[54] J. Fan, B. Li, S. Xing, T. Pan, Reconfigurable microfluidic dilution for high-throughput quantitative assays, Lab Chip 15 (2015) 2670–2679.
[55] T. Leighton, The Acoustic Bubble, Academic Press, 2012.
[56] S. Wang, X. Huang, C. Yang, Microfluidic bubble generation by acoustic field for mixing enhancement, J. Heat Transfer 134 (2012).
[57] M.G. Cain, M. Stewart, Piezoelectric resonance, in: M.G. Cain (Ed.), Characterisation of Ferroelectric Bulk Materials and Thin Films, Springer Netherlands, Dordrecht, 2014, pp. 15–35.
[58] M. Gresil, L. Yu, V. Giurgiutiu, M. Sutton, Predictive modeling of electromechanical impedance spectroscopy for composite materials, Struct. Health Monit. 11 (2012) 671–683.
[59] T. Kamas, V. Giurgiutiu, B. Lin, E/M impedance modeling and experimentation for the piezoelectric wafer active sensor, Smart Mater. Struct. 24 (2015), 115040.
[60] R.M. Finzi Neto, V. Steffen, D.A. Rade, C.A. Gallo, L.V. Palomino, A low-cost electromechanical impedance-based SHM architecture for multiplexed piezoceramic actuators, Struct. Health Monit. 10 (2011) 391–402.
[61] E.Sd. Freitas, F.G. Baptista, D.E. Budoya, B.Ad. Castro, Equivalent circuit of piezoelectric diaphragms for impedance-based structural health monitoring applications, IEEE Sens. J. 17 (2017) 5537–5546.
[62] Z. Shen, W.Y. Shih, W. Shih, Flexural vibrations and resonance of piezoelectric cantilevers with a nonpiezoelectric extension, IEEE Trans. Ultrason. Ferroelectr. Freq. Control 54 (2007) 2001–2010.
[63] C. Rugina, D. Enciu, M. Tudose, Numerical and experimental study of circular disc electromechanical impedance spectroscopy signature changes due to structural damage and sensor degradation, Struct. Health Monit. 14 (2015) 663–681.
[64] C.G. Khan Malek, Laser processing for bio-microfluidics applications (part I), Anal. Bioanal. Chem. 385 (2006) 1351–1361.
[65] C.G. Khan Malek, Laser processing for bio-microfluidics applications (part II), Anal. Bioanal. Chem. 385 (2006) 1362–1369.
[66] P. Nath, D. Fung, Y.A. Kunde, A. Zeytun, B. Branch, G. Goddard, Rapid prototyping of robust and versatile microfluidic components using adhesive transfer tapes, Lab Chip 10 (2010) 2286–2291.
[67] K.-A. Hyun, T.Y. Lee, S.H. Lee, H.-I. Jung, Two-stage microfluidic chip for selective isolation of circulating tumor cells (CTCs), Biosens. Bioelectron. 67 (2015) 86–92.
[68] S. Sun, M. Ossandon, Y. Kostov, A. Rasooly, Lab-on-a-chip for botulinum neurotoxin a (BoNT-A) activity analysis, Lab Chip 9 (2009) 3275–3281.
[69] Y. Liu, W. Wang, W. Hu, Z. Lu, X. Zhou, C.M. Li, Highly sensitive poly[glycidyl methacrylate-co-poly(ethylene glycol) methacrylate] brush-based flow-through microarray immunoassay device, Biomed. Microdevices 13 (2011) 769–777.
[70] M.I. Mohammed, M.P.Y. Desmulliez, Autonomous capillary microfluidic system with embedded optics for improved troponin I cardiac biomarker detection, Biosens. Bioelectron. 61 (2014) 478–484.
[71] Y.H. Tennico, D. Hutanu, M.T. Koesdjojo, C.M. Bartel, V.T. Remcho, On-chip aptamer-based sandwich assay for thrombin detection employing magnetic beads and quantum dots, Anal. Chem. 82 (2010) 5591–5597.
[72] P. Khashayar, G. Amoabediny, B. Larijani, M. Hosseini, S. Van Put, R. Verplancke, J. Vanfleteren, Rapid prototyping of microfluidic chips using laser-cut double-sided tape for electrochemical biosensors, J. Braz. Soc. Mech. Sci. Eng. 39 (2017) 1469–1477.
[73] J. Nestler, A. Morschhauser, K. Hiller, T. Otto, S. Bigot, J. Auerswald, H.F. Knapp, J. Gavillet, T. Gessner, Polymer lab-on-chip systems with integrated electrochemical pumps suitable for large-scale fabrication, Int. J. Adv. Manuf. Technol. 47 (2010) 137–145.
[74] J. Kim, Y. Shin, S. Song, J. Lee, J. Kim, Rapid prototyping of multifunctional microfluidic cartridges for electrochemical biosensing platforms, Sens. Actuators B Chem. 202 (2014) 60–66.
[75] A.W. Martinez, S.T. Phillips, G.M. Whitesides, Three-dimensional microfluidic devices fabricated in layered paper and tape, Proc. Natl. Acad. Sci. U.S.A. 105 (2008) 19606–19611.
[76] M. Yang, S. Sun, Y. Kostov, A. Rasooly, Lab-on-a-chip for carbon nanotubes based immunoassay detection of Staphylococcal Enterotoxin B (SEB), Lab Chip 10 (2010) 1011–1017.
[77] S. Prakash, S. Kumar, Fabrication of microchannels on transparent PMMA using CO2 Laser (10.6 μm) for microfluidic applications: an experimental investigation, Int. J. Precis. Eng. Manuf. Technol. 16 (2015) 361–366.
[78] J.P. Davim, N. Barricas, M. Conceição, C. Oliveira, Some experimental studies on CO2 laser cutting quality of polymeric materials, J. Mater. Process. Technol. 198 (2008) 99–104.
[79] D. Kim, D.H. Son, D. Jeon, Feed-system autotuning of a CNC machining center: rapid system identification and fine gain tuning based on optimal search, Precis. Eng. 36 (2012) 339–348.
[80] C. Chindam, N. Nama, M.I. Lapsley, F. Costanzo, T.J. Huang, Theory and experiment on resonant frequencies of liquid-air interfaces trapped in microfluidic devices, J. Appl. Phys. 114 (2013), 194503.
[81] K. Uchino, Chapter 1 - the development of piezoelectric materials and the new perspective, in: K. Uchino (Ed.), Advanced Piezoelectric Materials, second edition, Woodhead Publishing, Cambridge, 2017, pp. 1–92.
[82] X. Dong, T. Yuan, M. Hu, H. Shekhani, Y. Maida, T. Tou, K. Uchino, Driving frequency optimization of a piezoelectric transducer and the power supply development, Rev. Sci. Instrum. 87 (2016), 105003.
[83] J. Erhart, P. Půlpán, M. Pustka, Piezoelectric Ceramic Resonators, Springer, Switzerland, 2017.
[84] N. Pérez, F. Buiochi, M.A. Brizzotti Andrade, J.C. Adamowski, Numerical characterization of piezoceramics using resonance curves, Materials 9 (2016) 71.
[85] K.A. Mirgissa, W. Lee, D. Kim, Toward rapid prototyping of high-aspect-ratio sub-100-μm PMMA microfluidic devices: optimization of CO2 laser machining and solvent-assisted thermal bonding, 2019 IEEE 32nd International Conference on Micro Electro Mechanical Systems (MEMS) (2019) 384–386.
[86] M. Mohammed, E. Abraham, M. Desmulliez, Rapid laser prototyping of valves for microfluidic autonomous systems, J. Micromech. Microeng. 23 (2013), 035034.
[87] M. Mohammed, M. Desmulliez, The manufacturing of packaged capillary action microfluidic systems by means of CO2 laser processing, Microsyst. Technol. 19 (2013) 809–818.
[88] H. Becker, L.E. Locascio, Polymer microfluidic devices, Talanta 56 (2002) 267–287.
[89] W. Sui, D. Zhang, Four methods for roundness evaluation, Phys. Procedia 24 (2012) 2159–2164.
[90] M. Pustka, L. Půst, Spectral properties of circular piezoelectric unimorphs, Arch. Acoust. 42 (2017).
[91] Y. Hu, X. Liang, W. Wang, A theoretical solution of resonant circular diaphragm-type piezoactuators with added mass loads, Sens. Actuators A Phys. 258 (2017) 74–87.
[92] X. Li, W.Y. Shih, I.A. Aksay, W.-H. Shih, Electromechanical behavior of PZT-brass unimorphs, J. Am. Ceram. Soc. 82 (1999) 1733–1740.
[93] L. Beranek, T. Mellow, Chapter fourteen - vibroacoustics (membranes, plates, and shells), in: L. Beranek, T. Mellow (Eds.), Acoustics: Sound Fields,

Transducers and Vibration, 2nd ed., Academic Press, Cambridge, 2019, pp. 721–789.
[94] M.G. Silk, Ultrasonic Transducers for Nondestructive Testing, United States, 1984.
[95] N. Guo, The Vibration Characteristics of Piezoelectric Discs, University of London, 1989.
[96] S.M. Heinrich, I. Dufour, Fundamental theory of resonant MEMS devices, in: O. Brand, I. Dufour, S.M. Heinrich, F. Josse (Eds.), Resonant MEMS, Wiley-VCH Verlag, Weinheim, 2015, pp. 1–28.
[97] W. Pang, H. Zhao, E.S. Kim, H. Zhang, H. Yu, X. Hu, Piezoelectric microelectromechanical resonant sensors for chemical and biological detection, Lab Chip 12 (2012) 29–44.
[98] A. Hashmi, J. Xu, On the quantification of mixing in microfluidics, J. Lab. Autom. 19 (2014) 488–491.
[99] S. Prakash, S. Kumar, Experimental and theoretical analysis of defocused CO2 laser microchanneling on PMMA for enhanced surface finish, J. Micromech. Microeng. 27 (2016), 025003.
[100] G. Nader, E.N. Silva, J.C. Adamowski, Effective Damping Value of Piezoelectric Transducer Determined by Experimental Techniques and Numerical Analysis, ABCM Symposium Series in Mechatronics, Rio de Janeiro, 2004, pp. 271–279.
[101] G.K. Fedder, C. Hierold, J.G. Korvink, O. Tabata, Resonant MEMS: Fundamentals, Implementation, and Application, John Wiley & Sons, 2015.
[102] K.A. Mirgissa, H. Jeon, D. Kim, A microfluidic cavitation-microstreaming DNA extractor, in: The 24th International Conference on Miniaturized Systems for Chemistry and Life Sciences, Basel, Switzerland, 2019, pp. 1560–1561.

Biographies

Hyunjin Jeon is an assistant engineer at Inventage Lab and a Master's student in the Department of Mechanical Engineering at Myongji University, South Korea. She is expected to receive her degree in 2021. Her research interest includes lab-on-a-chip, laser microfabrication, and ultrasonic actuation.

Kaba Abdi Mirgissa is a Ph.D. student in the Department of Mechanical Engineering at Myongji University. He received his B.S. and M.S. degrees in Mechanical Engineering from Addis Ababa University, Ethiopia in 2015 and 2017 respectively. His research interest includes microfluidics, optimization of polymer-based microfabrication processes, and microfluidic lab-on-a-chip devices for biomolecular analysis.

Seonhyeok Baek is a Master's student in the Department of Mechanical Engineering at Myongji University, South Korea and is expected to receive his degree in 2022. His research interest includes microfluidics, laser microfabrication, and MEMS (Micro-Electro-Mechanical-Systems) electrolytic actuators.

Kyehan Rhee received his B.S. degree from Seoul National University and his Ph.D. degree from University of Minnesota in Mechanical Engineering in 1984 and 1990, respectively. His research interests include hemodynamics, tissue mechanics, microfluidics and their application in biomedical devices. He is currently a professor of the department of mechanical engineering at the Myongji University in Korea.

Dohyun Kim is an associate professor in the Department of Mechanical Engineering at Myongji University, South Korea. He received a B.S. and M.S. degrees in Mechanical Engineering from Sogang University, South Korea in 1993 and 2001, respectively. He graduated from the University of California, Los Angeles, United States in 2008 with a Ph.D. degree in Electrical. Before starting his professorship at Myongji University, he worked as a postdoctoral scholar in the Bioengineering Department at the University of California, Berkeley for 3 years. His research interest includes polymer microfabrication, MEMS actuators, and microscale bioanalytical systems for disease diagnostics.